UAB

Treball de Fi de Grau

Grau en Enginyeria de Sistemes de Telecomunicació

Frequency-modulated continuous-wave radar in automotive applications

Eloi Guerrero - Menéndez

Director: Pedro de Paco Sánchez

Departament de Telecomunicació i Enginyeria de Sistemes

Universitat Autònoma de Barcelona

Bellaterra, Juliol 03, 2018

Abstract

Although initially linked to the military world, radar technology is at its best. Due to both great advances in electronic devices miniaturization and to economic and social interest in increasing automotive safety, mounting radar modules on-board day-to-day vehicles is now a reality. These new safety needs and the transition towards the so-called *connected vehicle* make the development of new radar-based solutions an attractive field of study.

In this project, the theoretical aspects on which the frequency-modulated continuous-wave radar is based, will be treated. Such an approach is the widespread solution in automotive applications. Additionally, the characterization of the *Demorad* platform from Analog Devices will be presented and supported measurement and operation modes will be explained. In terms of experimental test, this project will be based on measuring inside an electromagnetic anechoic chamber that will enable acquisition and analysis of the main radar observables: range, velocity and angular position. Finally, the implementation of a low-cost target emulator focused on the hardware-in-the-loop philosophy will be presented.

Resum

Tot i ser inicialment lligat al món militar, la tecnologia radar es troba en un dels seus millors moments. Degut a grans avenços en la miniaturització dels dispositius electrònics i a l'interès econòmic i social per augmentar la seguretat del sector automobilístic, l'embarcament de radars en els vehicles d'ús diari és una realitat. Aquestes noves necessitats de seguretat i la transició cap al famós *vehicle connectat* fan del desenvolupament de noves solucions basades en sistemes de radar un camp d'estudi atractiu.

En aquest projecte es tractaran inicialment els aspectes teòrics que fonamenten el tipus de plataforma utilitzat en l'automoció: el radar d'ona contínua modulat en freqüència. Alhora, es presentarà la caracterització de la plataforma *DemoRad* d'Analog Devices i s'explicaran els modes d'operació i mesura que suporta. El marc experimental d'aquest projecte es basarà en mesures dins d'una cambra anecoica electromagnètica que permetran demostrar l'obtenció i l'anàlisi dels principals observables d'un radar: la distància, la velocitat i la posició angular. Per acabar, es mostrarà la implementació del prototip d'un emulador de blancs de baix cost enfocat a la simulació dinàmica d'obstacles seguint la filosofia del *hardware-in-the-loop*.

Acknowledgements

I would like to thank Prof. Pedro de Paco for giving me the opportunity of working at the Antenna and Microwave Systems (AMS) Group laboratory and having such a good time learning new things. I also want to thank the rest of AMS members, Josep Parrón, Jordi Verdú and Gary Junkin for patiently answering my long list of random questions. Finally, thanks to Ernesto Díaz for carefully milling and soldering the built devices.

Always remember to turn on the DC supply

— Anonymous

Contents

List of Figures

List of Tables

Glossary

The radar field has an extensive vocabulary that sometimes can lead to confusion. In this glossary some words and the usage of some terms in this project are explained.

Terms

- **Range and distance** Although initially used with different meanings, range meant the round-trip and distance the single trip, both terms are now used in conjunction to refer to the displacement from the radar to the target, in metres.
- **Transmitters** Within this project different terminology is used to refer to the transmitter antennas. Either *TX* or *transmitter* can be found in this document.
- **Receivers** As with transmitters, in order to refer to the 4 receiver antennas of the board, either *RX*, *receiver* or *channel* is used.

Acronyms

- **UWB** Ultra wide band
- **IF** Intermediate frequency.
- **LO** Local oscillator.
- **FFT** Fast Fourier transform.
- **DoA** Direction of arrival.
- **MSPS** Megasamples per second.
- **SSB** Single-sideband (mixer).
- **USB/LSB** Upper sideband / lower sideband.

Chapter 1

Introduction

Although normally linked to military and law enforcement applications due to its development, RADAR is nowadays a widespread solution for civil situations. The term itself was initially coined by the US Navy as an acronym for Radio Ranging and Detection (hereafter written without capitals) and was firstly developed in parallel by Germany, Great Britain and the US, prior to World War II (WWII).

As a short historical introduction to radar one must head back to Christian Hülsmeyer and his *Telemobiloskop*, an invention patented in 1903 that was aimed to prevent ship collisions in foggy conditions. The invention was based on Heinrich Hertz discoveries on the reflection of EM waves on metallic surfaces. Hülsmeyer is usually credited with the invention of radar eventhough his patents were unknown to the next generation of engineers that developed real military radar deployments in the 30's [Sar14]. Different events triggered the discovery of radar for each of the different teams working on detection systems, and Rudolph Kühnold (German Navy), Rober Watson-Watt (British Army) and Robert M. Page (US Navy) are considered the developers of radar in their respective countries. The use of German *Freya*, *Würzburg* and *Seetakt* systems and the fast deployment of british *Chain Home* were key factor for the evolution of WWII, and the need to counterfeit enemy systems lead to huge efforts on microwave technologies research. These efforts made possible all the applications that were developed from the 50's onwards. Once WWII was ended, parallel to further improvement of military radar, civilian focused applications such as weather forecasting, surveillance for civilian aviation or ship collision avoidance were conceived but technological constraints made these systems unable to be widely marketed. For example, power requirements made portable detection devices almost impossible. In the 70's, thanks to significant advances, first tests on automotive radar were performed and were the first steps into a whole new field of research that is nowadays trending. Today, connectivity and *smart* devices drive our lives and are changing the paradigm. The initially sci-fi concept of a self-driven car is now real and relies on the performance of an specific system: radar.

1.1 Automotive safety

More than 1.2 million people die in traffic accidents each year worldwide making it the main cause of death among young people [WHO15]. At the same time, road accidents are estimated to cost an average of 3% of world's GDP. In the case of Spain, the total cost (including public health system data) is estimated around 9.25 billion Euro, which means approximately 1% of the country's gross domestic product [Coo17]. This numbers are a great concern for both governments and the automotive industry: the firsts assume a big part of the overall cost of accidents and automotive industry fears a change on how society conceives cars and their dangers. They do not want to be considered a dangerous means of transportation and it is to be remarked that automotive is one of the biggest industries worldwide; specifically in Spain, where almost 300,000 people are employed in the automotive sector. These fears have been the motive behind investments in advanced security technologies in the last decades and are pushing towards an scenario where there are no automotive-related fatalities. Companies are looking for an equilibrium between investing in security systems, meeting demand of these solutions and getting ready for an expected regulation making these systems mandatory. EU program *Horizon 2020*, under the slogan *2011 - 2020: the decade of action for road safety* sets radar sensors and cameras for autonomous driving as a key topic to be funded.

From a historical point of view, as early as in 1970, first solutions started to be developed and new terms such as Long Range Radar (LRR), short range radar (SRR), Blind Spot Detection (BSD) or Lane Change Warner (LCW) were coined. First experimental systems appeared in the early 1970's but it was not until 1998 that Mercedes-Benz released the 77 GHz *DISTRONIC* system that was followed in 2006 by *DISTRONIC PLUS*, the first series-produced automotive radar system. It featured a 77 GHz LRR sensor and two 24 GHz SRR sensors [Mei14]. Since then, most automotive manufacturers have adopted radar systems not only for premium cars but for all their vehicles. New security solutions such as Adaptive Cruise Control (ACC) or Automatic Emergency Braking (AEB) are now possible and suppose a revolution. The aforementioned systems are normally referred to as ADAS (Advance driver-assistance systems) and include a vast range of applications that aim to help and guide the driver to avoid accidents and dangerous situations: forward collision avoidance, parking sensors or pedestrian protection systems. The objective behind all this technology is making the vehicle capable of interacting with its surrounding elements to counter human limitations such as reaction times. Although ADAS have since long been a hot topic, it has not been until the last decade that companies have invested large amounts of money, and this has been possible due to the development of new communication technologies that allow the conception of a key idea: connected vehicles. The release of LTE - Advanced and the growing interest and expectations on the so-called 5G have created an internet of things (IoT) fever in which everybody dreams of a near future where all devices are connected: from the fridge to the blinds. This connectivity is actually tangible for

Sensor	Strengths	Weaknesses
Infra-red (IR)	Low cost. Wide FOV. Short range designed.	Rain and dust affected. No velocity measurement
Ultrasound (US)	Low cost and short range designed.	No angular resolution. Noise and wind affected
Laser	High directivity. Excellent choice for range	Rain and fog affected
Camera	Good FOV. Average max. range.	No velocity data
Radar	Good under all weather conditions. Range up to 250 m. Good cost.	No object classification.
Lidar	Best velocity and range resolution	High cost

Table 1.1: Comparison between available sensing technologies

cars and now it is not uncommon that a new car is equipped with a SIM card that allows it to connect to the Internet and recover information. Companies want to exploit this connectivity in order to improve car performance and fulfil clients expectations. Vehicles that communicate with each other and that can drive themselves based both on on-board systems (like radar) and incoming information from the Internet are proposed. This is the actual driver of the automotive market: the need for better and more reliable safety systems that are cheap to deploy.

1.1.1 Available sensing technologies

In order to describe the importance of radar systems applied to automotive situations and the reasons behind choosing it as a key system, a comparison study between other available sensing systems is described. As seen in table 1.1, other solutions for sensing vehicle surroundings include infra-red, ultrasound, lasers, cameras, radar and lidar, and for each of them, different performance metrics have been evaluated, for example, maximum range, field of view (FOV), weather affectation and economical viability.

1.2 Spectrum regulation

Two frequency bands were initially allocated for radar applications: the 24 and the 77 GHz bands. The hardware limitations of the 77 GHz band made it complicated for the development

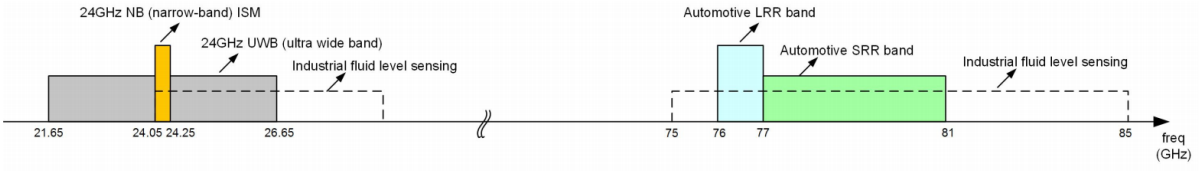

Figure 1.1: Radar frequency spectrum allocation

of novel solutions and in the beginning some systems were deployed at the lower band. The 24 GHz band is an unlicensed band that was initially divided in an ISM (Industrial, scientific and medical) band of 250 MHz from 24 to 24.25 GHz and an ultra wide band (UWB) from 21.65 to 26.65 GHz. Although initially dedicated to radar, due to the increasing development of 5G technologies, the ultra wide band was phased out by the ITU, setting the "sunset date" on 2021 [Ram17]. This decrease in bandwidth made the remaining ISM band unattractive for automotive radar and most solutions have shifted to the higher 77 GHz band. Figure 1.1 depicts the frequency allocation along the two bands.

As it will be shown later on in this project, range resolution and accuracy are inversely proportional to the bandwidth in automotive radar sensors. Thus, the shift from 24 to 77 GHz supposes an improvement of almost a factor 20 in terms of range resolution, as it is proportional to the swept bandwidth, and an improvement in velocity resolution by a factor of 3, as it is inversely proportional to the frequency. However, not only the automotive sector is shifting towards the higher band, also other industrial applications such as industrial liquid-level sensing or UAV (unmanned aerial vehicle) altimeters are being adapted to the new band. From the automotive point of view, the higher band is also interesting in terms of reducing hardware size and because the higher attenuation due to propagation, reduces the potential interferences with other vehicles.

Chapter 2

Radar theory

In this chapter a theoretical introduction to radar and a thourough explanation of FMCW radar is presented. The three main radar observables: range, velocity and direction of arrival, and other key figures such as the radar cross section, are treated in terms of maximum achievable values and minimum resolution.

2.1 The concept of radar

Imagine the situation of someone throwing a pebble into a well and listening to sound it produces. From the time delay between throwing the pebble and the sound, an approximation of the well's depth can be made. This simple case might be every child first contact with the radar concept as it is based on the same principle: emitting electromagnetic waves and "listening" to the echoes coming from objects these waves have collided with. In general, radar systems can provide many observables such as range[1], velocity, target size and target angle, and therefore the physical and mathematical foundations that allow this observables has to be introduced. At the same time, radar performance capabilities strongly depend on a wide range of factors such as the emitted waveform or the bandwidth, and hardware limitations such as the physical size of antennas. In order to give an accurate but simple idea of this topics, the two main approaches to radar systems have to be explained.

Initially, the most intuitive approach to the radar concept might be the pulsed one. Emitting an electromagnetic pulse and receiving its echoes seems a rather simple assumption. Range information can then be extracted from time delay or power measures. However, some drawbacks to this approach exist and will be discussed later on in this section. The second approach consists

[1] In the radar community, the term range is either used to refer to the whole round-trip distance travelled by the wave or to the real distance at which the target is located. In this project, the intention is to use range and distance as the real position value. Specific cases, if any, will be noted.

on emitting continuous waveforms so that range information is extracted from the frequency component induced by the time delay when mixing with a reference signal. Different frequency-modulated waveforms are used in continuous wave (CW) systems, such as linear chirp sequences or triangular waveforms. The CW strategy has some drawbacks as will be discussed later on, but its features do fit requirements well. As a first step, before diving into the depths of radar theory, a first essential metric needs to be presented: radar cross section (RCS).

2.1.1 Scattering

Radar performance lies on the reception of electromagnetic waves reflected from targets and thus the phenomenon of scattering plays a fundamental role. Scattering is a physical process through which some forms of radiation deviate from their trajectory due to meeting obstacles such as singular particles or non-uniformities in the propagation medium. Electromagnetic waves are scattered when they meet with an obstacle and the scattered waves originate from the obstacle's position. Therefore, any illuminated obstacle appears as a transmitter with its transmit power being directly proportional to the incident (illuminating) power density S. A factor modelling the relation between reflected power and incident power density is called radar cross section (RCS) and denoted by σ. It has units of square meters and depends on the direction of incidence, the direction of scattering, material properties of the obstacle and the wavelength. Figure 2.1 shows a usual bistatic scattering case. Bistatic means that emission and reception locations are not the same and monostatic means that emitter and receptor are at the same position.

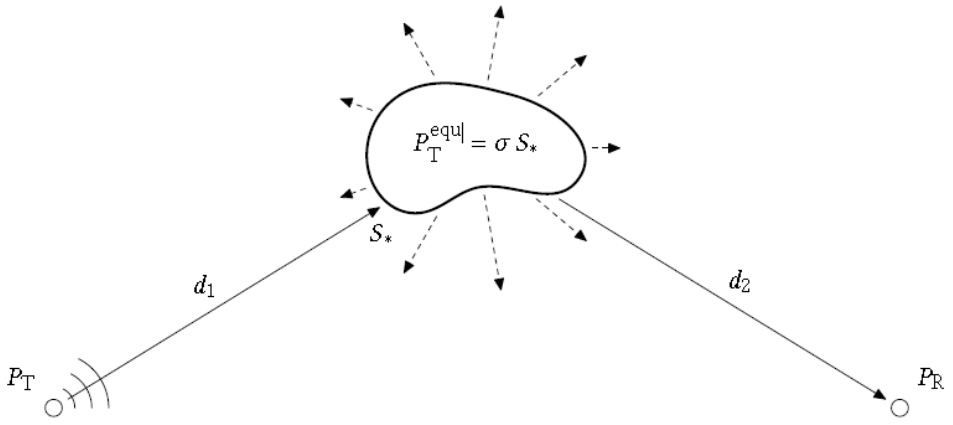

Figure 2.1: Bistatic scattering case.

Wavelength influence on RCS is strong as it is responsible for *electric* size of objects. This means, how big is a target in terms of wavelength λ. Figure 2.2 shows the typical plot of the RCS of a PEC (perfect electric conductor) sphere. See that there are 3 main scattering regions: Rayleigh, resonant or Mie, and optical. The Rayleigh region is the one related to objects that

are small in terms of wavelength and the evolution of RCS in this region, is proportional to $1/\lambda^4$. The maximum RCS is achieved in the Mie resonant region where the resonating behaviour is due to diffraction and interference between impinging and reflected waves. Finally, RCS converges to an stable value as objects become electrically large and act as a flat surface in terms of reflection. Note that fluctuations of RCS on wavelength may give an idea of another important issue to consider when designing radar systems: operation frequency has an influence on how large targets to be detected can be.

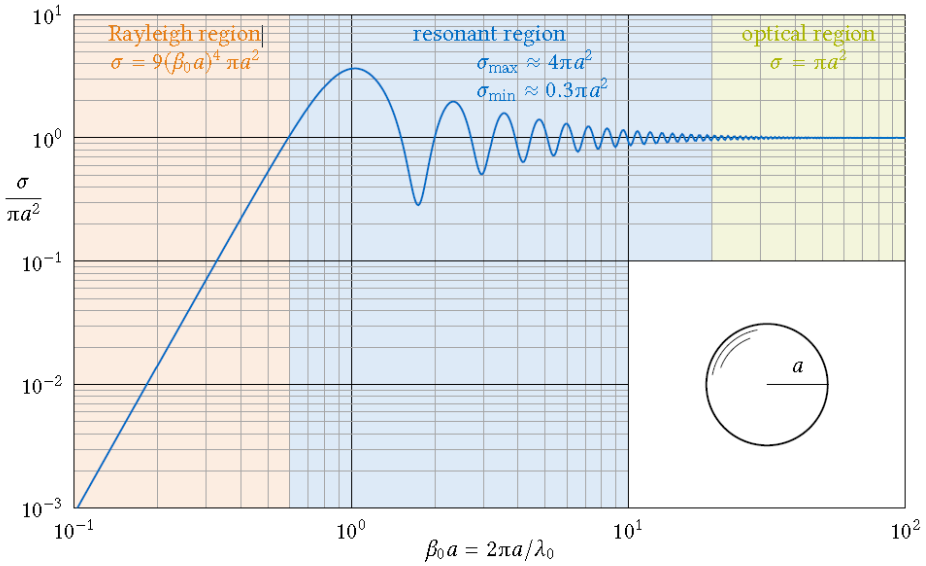

Figure 2.2: Backscattering RCS of a PEC sphere. [Sia18]

2.1.2 Radar range equation

When the scattering phenomenon is considered, the next step to take into account is the path between transmission antenna and the target itself. Recalling Friis transmission formula, incident power density on target can be modeled as follows,

$$S_i = \frac{GP_{TX}}{4\pi r^2} \tag{2.1}$$

where G is the antenna gain, P_T is transmitted power and factor $4\pi r^2$ models the surface of the sphere in which energy is radiated. Given $\sigma = P_{scattered}/S_i$, and $A_{eff} = \frac{G\lambda_0^2}{4\pi}$ (the effective aperture of the antenna), the received power can be assumed as the propagation of backscattered power, yielding the well-known radar range equation in (2.2).

$$\frac{P_R}{P_T} = \frac{G^2\lambda_0^2\,\sigma}{(4\pi)^3 r^4} \tag{2.2}$$

From the previous equation the first range measurements can be extracted by comparing received and transmitted power. See that path losses and antenna gain are taken into account twice as propagation takes place forth and back.

2.1.3 Pulse radar

The well example at the beginning of this section is an analogy of the so called pulse radar, because the way to achieve range measurement is transmitting pulses and waiting for backscattered echoes to reach the radar. Range is then extracted from the time delay between transmission and reception. The specific features of these systems are mainly bounded by the time duration of the pulse and its repetition frequency. For example, range resolution Δr, that is the minimum distance between two targets so that they are resolved as different objects, is limited by pulse duration because pulses must not overlap to be correctly resolved. Other well known figures that are inherent to radar systems can be the unambiguous range R_{unam}, the maximum range at which there is no ambiguity to link transmitted pulses and the respective echoes, that in the case of pulse radar, is limited by the pulse repetition frequency (PRF). In order to tackle some of this limitations, specific techniques such as pulse compression have been developed for pulse radar but these are out of scope in this project because they do not fit automotive sector requirements. Pulse transmission means short high-power bursts combined with echo listening times, which might not be the optimal solution for a highly dynamic environment as the automotive. At the same time, achieving high peak power requires from specific hardware (mainly high power oscillators such as klystrons or magnetrons) that can not scale down to fit behind the bumper of a vehicle. Another drawback for the pulse-based approach is that these systems provide hardly any information about target velocity.[2] These makes this systems suitable for meteorology and long range surveillance but velocity information is a major requirement in the automotive field. Further explanation on these topics can be found in classical books such as *The radar handbook* by Merrill Skolnik [Sko08].

2.1.4 Continuous wave radar

The opposite solution to the one based in short pulses is emitting a continuous waveform and thus avoid high-power bursts and the related constraints. The simplest type of continuous wave (CW) radar is one that detects target velocities. The main idea is to transmit a sinusoidal signal and receive the resulting backscattered tone. Because of the Doppler effect, any radial velocity

[2]Since the 1970's Pulse-doppler radar systems have been developed as an integration of both continuous wave and pulsed radar systems. This type of radars are widely deployed in military aircraft and are the actual trend in high budget applications. However they do fall out of scope in the automotive radar field due to size, power and cost limitations.

component present in the target supposes an added Doppler shift to the backscattered signal frequency. Then, when mixed with the transmission reference signal, the received one yields a simple tone at f_d. Doppler frequency maps to velocity as in (2.3) considering that factor 1/2 accounts for forth and back propagation, and that f_d is Doppler frequency, c_0 is the speed of light in vacuum and f_c is the carrier frequency.

$$v_r = \frac{f_d c_0}{2 f_c} \tag{2.3}$$

See that this mode of operation provides no information about range (there are no time instants to be compared) and that there is neither any information about the target departing or approaching the radar due to the fact that the two possible Doppler frequencies for a specific velocity are the image frequency of each other ($f_c + f_d,\ f_c - f_d$). They are down-converted to the same f_d absolute value and movement direction cannot be inferred. To solve this situation an IQ down-converter can be used. Both output signals can be represented as a phasor and the sign of the velocity can be extracted from the rotation direction of it. If the phasor rotates clockwise (mathematically negative) the target departs from the radar, if counter-clockwise (mathematically positive) the target approaches the radar.

Compared to pulsed systems, the system complexity is smaller as there is no need to handle high transmission power peaks and additionally, CW systems are highly sensitive to small changes in the observed scenario because phase variations can be detected, what makes them interesting in the field of automotive radar. However, the main drawback is that range information is lost [Sko08]. Thus, the need for a radar system that can resolve both speed and range is finally approached by a sort of junction between the two previously mentioned schemes.

2.2 Frequency-modulated continuous-wave radar

The reason why CW radar is not able to provide range information is the lack of a time marking strategy that could allow distance calculation and as said before, ranging using pulses is achieved by inferring the distance from time delay between transmitted pulse and echoes. Therefore, a combination of both can be achieved by means of frequency modulated signals such as sawtooth, triangular or stepped frequency. Before going deep into the explanation of the different waveforms, it is interesting to present the FMCW system. Figure 2.3 shows a rather simple example of such a system, that in essence will consist on a FM signal source, separate transmit and receive antennas and a signal processing chain that will perform the computations explained in the following sections.

Concerning the frequency modulated waveforms, these type of modulations consist on using chirp signals, or in other words, signals whose frequency increases linearly with time. A simple

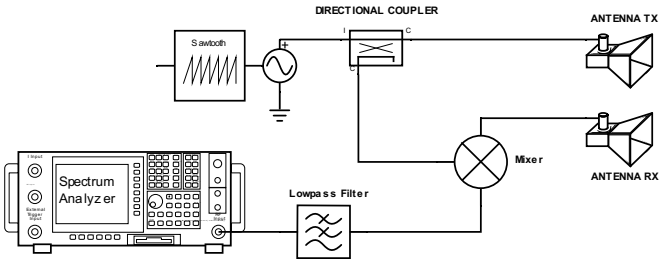

Figure 2.3: FMCW system sketch

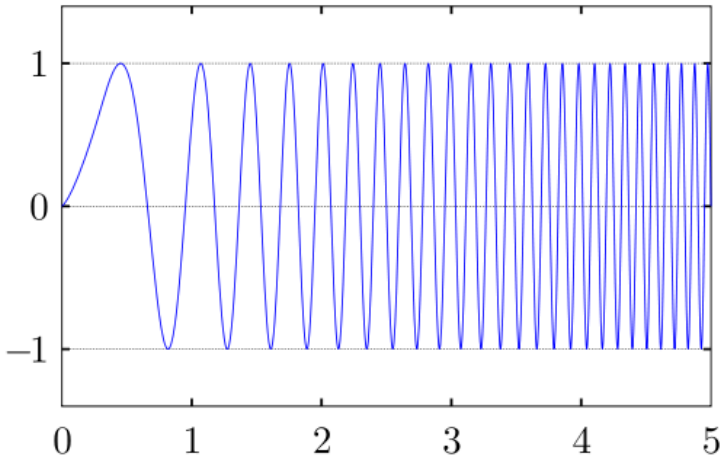

Figure 2.4: Chirp waveform

chirp (see figure 2.4) is a frequency ramp and its instantaneous frequency can be expressed as in (2.4), where B is the swept bandwidth and T_{sweep} is the time duration of the ramp. A concatenation of chirps will then form a sawtooth modulation, which is the basis for frequency modulated continuous wave (FMCW) radar operation. Frequency modulation is, additionally, an interesting scheme because by avoiding an envelope modulation, amplifiers can operate in saturation regime without causing major problems.

$$f(t) = f_0 + \frac{B}{T_{sweep}}t \tag{2.4}$$

Before going into the explanation of computation of observables, it is interesting to provide an explanation of the general operation behind FMCW. So, let us assume that there is an static obstacle in front of a chirp-emitting radar. As expected, the emitted wave will travel to the target and due to scattering, will propagate back to the receiving antenna. The chirp will be received and the differences with respect to the emitted one will be a certain delay and attenuation. This attenuation factor is directly related to the RCS of the target and although it is not the main

topic of this project, it is interesting to point that it is possible to study how do certain objects behave in terms of RCS to find signatures and patterns for object identification.

In this case the focus is on the range information and it will be extracted from the delay factor that appears with respect to the reference chirp. In figure 2.5, a visual explanation of how do chirps provide range information is shown. Due to propagation round-trip delay, the two chirps are in a different point of the slope for a given moment in time. Thus, this difference in instantaneous frequency will yield a single-frequency tone if both signals are mixed, because a mixer outputs the difference and the sum of the radio frequency (RF) and the local oscillator (LO) frequencies[3].

2.2.1 Range computation

In the previous straightforward explanation it has been shown that a time delay between two frequency ramps that are mixed will yield a constant frequency tone. This IF tone is related to the chirp ramps as in (2.5) and the round-trip delay is directly related to the distance (R) as $t_{delay} = c_0 \cdot R/2$. With this, the equations from which the range is extracted are found.

$$f_{TX} - f_{RX} = f_{IF} = \frac{B}{T_{sweep}} \tau_{delay} \tag{2.5}$$

$$R = \frac{c_0 \ f_{IF} \ T_{sweep}}{2 \ B} \tag{2.6}$$

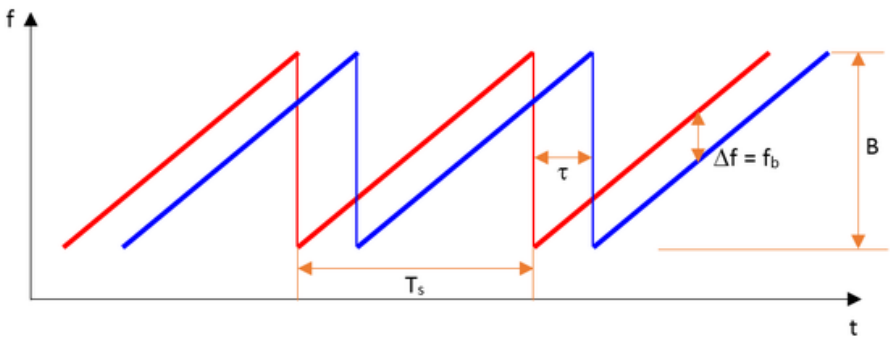

Figure 2.5: Relation between delay and IF tone

However, in a real situation it is not so simple to obtain the IF value; the real measured data will yield *sinc*-like spectral components at certain bins that refer to range. In the radar module, the IF sinusoid that results from mixing will be sampled and in order to find the value of the

[3]From now on, this intermediate frequency will be referred as IF as it is the output of a mixing stage.

frequency, an FFT (Fast Fourier Transform) will be applied. The FFT algorithm is a fast way to compute the Discrete-Time Fourier Transform that extracts frequency components from a set of n time-domain samples, and this algorithm is computed by the radar module for each of the received chirps. Ideally for an static target, the desired FFT output would be a Dirac delta at the exact IF frequency. However, the fact that the sinusoid is finite (i.e. windowed in time) will yield a convolution with a *sinc* function in the frequency domain, the main lobe width of which is directly related to the amount of samples taken from the sinusoid (the time duration of the window). The first zero of this *sinc* function appears at $1/T_{window}$ and this means that the radar will only be able to separate frequency components that are at least spaced by $\Delta f = 1/T_{window}$. If the frequency spacing is evaluated into equation 2.5 and noting that T_{window} is T_{sweep}, the expression for the range resolution is achieved in (2.7).

$$\Delta R = \frac{c_0}{2B} \tag{2.7}$$

The assumption until now was that a single static target was present in front of the radar, so range resolution was not really considered in the explanation. However, radar sensors are designed to cope with crowded environments and multiple targets in range and thus, the minimum distance at which the radar can distinguish between two targets becomes important. See also that the ability to separate close targets only depends on the swept bandwidth and therefore, larger bandwidths yield better resolutions. This is one of the main triggers for the change to 77 GHz operation frequency as the available bandwidth in that band is 4 GHz.

On the other hand, also the maximum range (also called unambiguous range) is a figure to study and it will be limited by the full-power bandwidth of the analog-to-digital converter of the radar. The ADC will have to sample an IF sinusoid whose frequency will be proportional to the range and in order to avoid aliasing, the Nyquist criteria must be fulfilled. The maximum IF frequency that is resolvable by the radar module will then be $f_s/2$ where f_s is the sampling frequency of the ADC. If this maximum IF frequency is evaluated in (2.5) the following is obtained:

$$R_{max} = \frac{c_0 \ f_s \ T_{sweep}}{4 \ B} \tag{2.8}$$

Some novel FMCW solutions have presented systems that do cope with signals for which the Nyquist sampling theorem is not fulfilled. This sparse data approach, for example by using the *l1-magic* algorithms, has been implemented in some radar systems related to compressive sensing. In a rather simple case of undersampling, for a given unambiguous range of for example 100 metres, some techniques can locate targets at range-chunks of 100 metres as long as the

reception power requirements are met. This solution falls out of scope in this project but has been found in the literature.

2.2.2 Velocity computation

The previous assumption considered that the target was static, but in case the target is a moving one, how will the radar perform? Will it be able to resolve the velocity of the target? If an static target yields an IF tone due to delay between reference and received chirps, note that for a moving target, this IF tone would be the superposition of two frequency components: the IF related to range and a Doppler component due to radial displacement between radar and target. Thus, the IF that results from the mixing stage can be modelled as in (2.9).

$$f_{IF} = \frac{B\ t_{delay}}{T_{sweep}} \pm \frac{2\ f_c\ v}{c_0} \tag{2.9}$$

Note that there are two different unknowns and one single equation, what makes the situation unsolvable. From a single chirp IF spectra, the Doppler information cannot be extracted as it is overlapping with the range IF component, but the use of the so-called *frame of chirps* gives a solution to this problem. The mentioned chirp frame is a set of consecutive chirps that are processed together to resolve both range and velocity. Note that the aim of a FMCW system is continuously transmitting and processing chirps, but at some point, the designer has to define how many of this chirps are going to be processed together (due to processor limitations and/or resolution factors).

Assume that a frame of Np chirps is emitted and arrives back at the radar module. The result will apparently be the same as before: the frame will be delayed with respect to the reference timing and each of the chirps will yield an IF tone that will be sampled and transformed to frequency domain in order to obtain a range profile. However, the key factor here is the phase of each of the IF tones. In terms of amplitude and frequency, all tones will almost be the same for each of the chirps in the frame, but as the target was moving, the phase of each tone will have changed continuously because the travelled distance has changed in-between chirps. Recall that the Fourier Transform is complex valued, yielding for each of the frequency bins, the amplitude of the sinusoid at that specific frequency (module of the complex number) and the phase of that frequency component.

$$X(k) = \sum_{n=0}^{N-1} x(n) e^{-j2\pi kn/N}$$

$$\angle X(k) = \arctan\left(\frac{Im(X(k))}{Re(X(k))}\right)$$

Therefore, after applying the FFT in range direction (i.e. to the n samples of the IF sinusoid), the different chirps spectra can be rearranged as a matrix, one range profile per column. The matrix will look like the one shown in figure 2.6, having $NFFT$ rows (where $NFFT$ is the amount of bins of the FFT) and Np columns. Now, another FFT in the second dimension (each of the rows) can be applied. The output of this transformation is the frequency spectrum related to the phase variations along chirps. Therefore, it is the Doppler spectrum. From this values, now the velocity information can be extracted using (2.3).

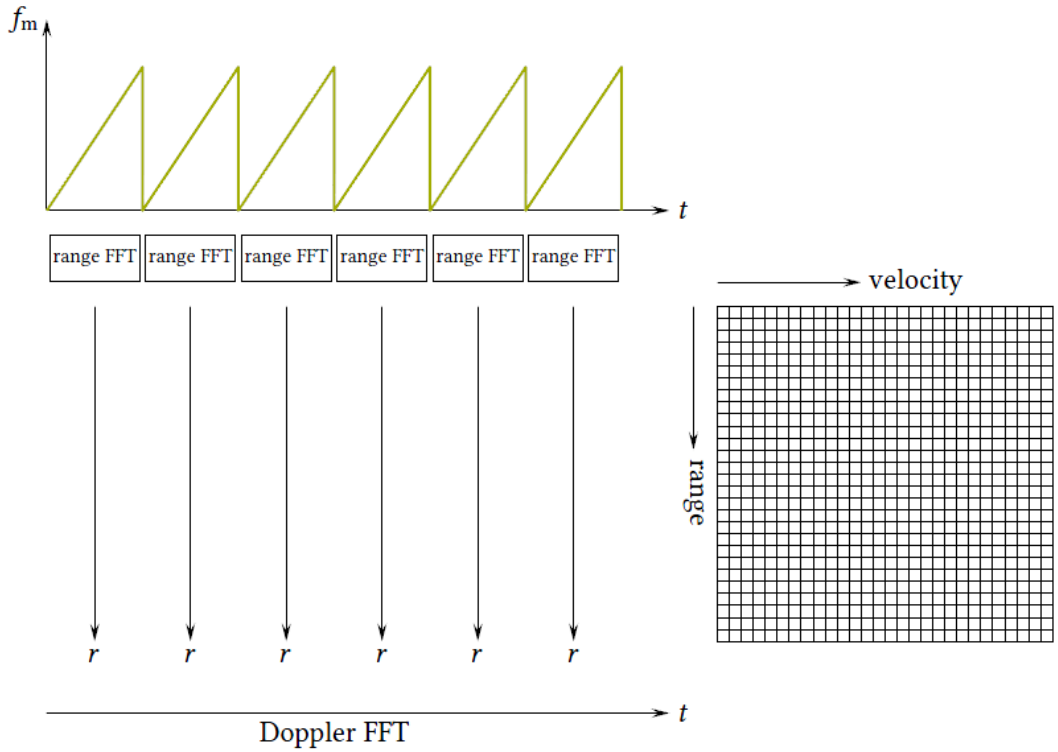

Figure 2.6: 2D FFT for Range-Doppler estimation [Sia18]

Mathematically, it is proven that both range and velocity can be jointly computed but some constraints need to be considered. See that what is being recovered from each of the different chirps is the phase at a certain point in time, and thus it can be interpreted as if each chirp is a sample of the time evolution of the phase. As usual, correct sampling involves fulfilling the Nyquist criteria so that there is no loss of information. This means that for a given chirp repetition time (that can be interpreted as the phase sampling frequency) there will be a maximum velocity that can be resolved unambiguously. This maximum detectable velocity is therefore limited to phase changes of up to $\pm\lambda/4$ in between chirps. It might seem confusing as Nyquist states that at most, the phase variation between two samples can be $\lambda/2$ but as radar handles forth and back propagation, a change in the target position of $\lambda/4$ will result in a change of $\lambda/2$ in the radar module. Applying the mentioned factors, maximum detectable velocity of a given radar can be stated as in (2.10).

$$v_{max} = \frac{\lambda}{4\ T_{sweep}} \tag{2.10}$$

It is important to note that maximum velocity is bounded by the chirp repetition interval T_{sweep} which means that faster chirps can map larger velocities[4]. However, fast ramps do require from high quality hardware if the swept bandwidth is to be maintained. For the same PLL ramp generator, decreasing T_{sweep} would mean sweeping less bandwidth and thus reducing range resolution; which is the first important trade-off in FMCW radar systems.

On the other hand, the velocity resolution will another time be limited by the amount of chirps that fit into a frame as Np will be the window size. See that the phase variation could be defined as follows,

$$\omega = 2\left(\frac{2\pi\ v\ T_{sweep}}{\lambda}\right) \tag{2.11}$$

where the factor 2 takes into account that the wave propagates forth and back. At the same time, the resolution in terms of phase is limited to $\Delta\omega = 2\pi/N_p$ because the minimum resolvable phase is that which sweeps a whole cycle in an entire frame of chirps. If both expressions are put together, the velocity resolution is defined as in (2.12).

$$\Delta v = \frac{\lambda}{2\ N_p\ T_{sweep}} \tag{2.12}$$

2.2.3 Direction of arrival computation

As a final point to this FMCW introduction, another important figure on automotive radar systems is to be considered. The described range and velocity joint computation can resolve two targets at the same distance that differ in velocity and these measurements can be performed by having only a pair of antennas: a receiver and a transmitter one. But what if it needs to resolve two targets at the same distance and velocity? This ambiguous situation can only be solved by computing the angular position of each target. See that it is of key importance that a radar sensor that aims to detect road obstacles and possible dangers, can accurately compute the direction of arrival (DoA) of the detected targets. Radars mounted in vehicles do have to create a map of all objects within their field of view in order to asses the aforementioned advanced driving assistance systems (ADAS), and this makes direction of arrival (DoA) computation a must.

[4]Here T_{sweep} is considered assuming that one chirp starts at the exact moment the previous one finished, which is an assumption far from reality as will be shown in the next chapter.

As it is presented in many antenna lectures, the angle of arrival of an incident wave can be computed by using an array of antennas. The direction at which the angle can be resolved depends on the axis at which the antennas are spaced. Horizontal arrays can resolve azimuth angles and vertical arrays resolve in elevation. At this point, let us consider the situation shown in figure 2.7, where an electromagnetic wave arrives at an antenna array with a certain angle with respect to the normal of the array base line. See that when the wave arrives to the first antenna, it will have to travel a distance d to the next antenna, which will yield a phase difference between the signal captured by the first and the second elements. This phase difference is related to the distance by means of the phase constant $\beta = 2\pi/\lambda$ as follows, where θ is the angle with respect to the normal.

$$\phi = \beta\ \Delta d = \beta\ d\sin(\theta) \tag{2.13}$$

Each of the N_a antennas in an array, will receive a phase delayed copy of the same frame of chirps, that will be stored as a receive channel. Thus, each antenna of the array is acting as a sampler in the spatial domain and each of the channels is a sample of the spatial frequency (ν) of the wave. This spatial frequency is a physical variable defined as $\nu = 1/\lambda$, with units of cycles per metre, that defines the periodicity of propagation in space domain, exactly as the frequency (f), in cycles per second, does in time. One can relate time evolution of a periodic oscillation by means of frequency and time, and so can do the same with space evolution in terms of spatial frequency and wavelength.

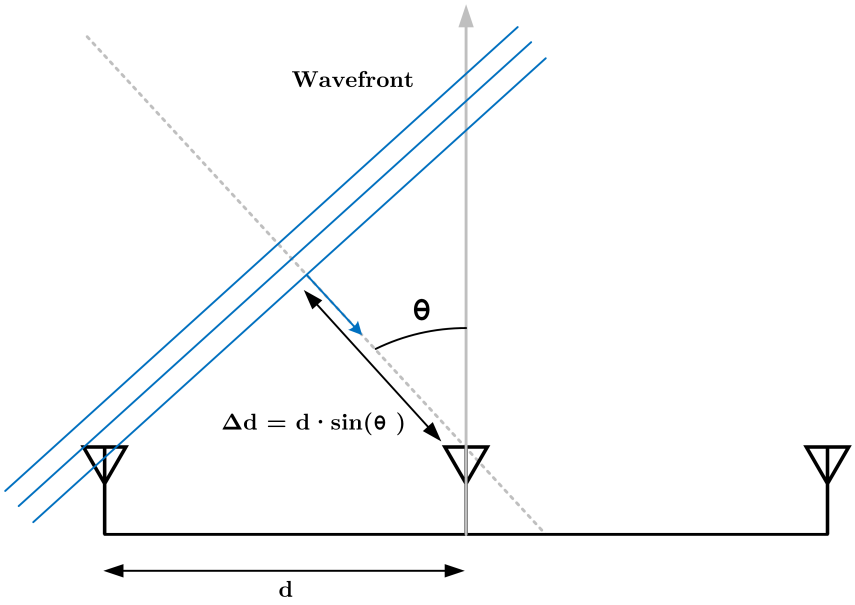

Figure 2.7: DoA antenna array model [PS18]

Back to the sampling nature of the antenna array, as shown in 2.2.2, from the Fourier

transform of n values in time, the frequency components of the signal were computed. Here, the same transformation holds but considering that index n refers now to spatial positions on a base line, and that the transformation yields the spatial frequency components of the signal. This is a transform to the spatial frequency domain or to the wave number domain if the factor 2π is considered. Therefore, peaks at certain spatial frequencies in this spectrum will convert to incident angles. See that now N_a is the amount of samples and the resolution of the DoA measurement is affected by the windowing effect of sampling. The angular resolution is limited by the length of the antenna array and can be defined as in (2.14).

$$\theta_{res} = \frac{\lambda}{N_a \; d \; cos(\theta)} \tag{2.14}$$

See that the angular resolution is defined in a single quadrant because of the geometry shown in figure 2.7. Thus, the angular resolution for a -90 to 90 degree map (two quadrants) will be doubled. Nevertheless, another important figure to study is the maximum field of view of the array. The well-known $\lambda/2$ spacing between antennas is the application of the Nyquist sampling theorem to spatial frequency: spatial sampling frequency must be at least 2ν to recover unambiguous angles of ± 90 degrees, which then yields that the spacing must be at least $\lambda/2$. See that,

$$\frac{2\pi}{\lambda} dsin(\theta) < \pi \rightarrow \theta_{max} = \arcsin\left(\frac{\lambda}{2d}\right) \tag{2.15}$$

Larger spacings would yield aliasing, thus reducing the total unambiguous field of view. Smaller spacing than half a wavelength would not result in wider angles but would not have a negative effect. However, spacing two antennas less than $\lambda/2$ is normally not possible because of physical size limitations. Note that antennas do normally span a length of $\lambda/4$ at each side of the phase centre.

As a final summary, table 2.1 groups all radar observables maximum values and resolutions to simplify the reading of this document if equations need to be revisited.

2.2.4 Other trends and solutions

In the previous sections the chirp frame approach to FMCW radar has been presented because it is the most widespread solution within the automotive and industrial sector solutions. However there are other frequency modulated waveforms that also yield very good results. For example, the stepped frequency FMCW consists on chirps that are not continuous in frequency but stepped in small constant steps. Another interesting proposal that was in use before the development of fast ramp FMCW (frame of chirps approach) was the triangular waveform. As it has been shown,

Radar equation	$\frac{P_R}{P_T} = \frac{G^2 \lambda_0^2 \ \sigma}{(4\pi)^3 r^4}$
Range R (m)	$R = \frac{c \ f_{IF} \ T_{sweep}}{2 \ B}$
Range resolution ΔR (m)	$\Delta R = \frac{c_0}{2B}$
Maximum range R_{max} (m)	$R_{max} = \frac{c \ f_s \ T_{sweep}}{4 \ B}$
Velocity v_r (m/s)	$v_r = \frac{f_d c_0}{2 f_c}$
Velocity resolution Δv (m/s)	$\Delta v = \frac{\lambda}{2 \ N_p \ T_{sweep}}$
Maximum velocity v_{max} (m/s)	$v_{max} = \frac{\lambda}{4 \ T_{sweep}}$
Angle of arrival resolution θ_{res} (degrees)	$\theta_{res} = \frac{\lambda}{N_a \ d \ cos(\Theta)}$
Field of view - FOV or θ_{max} (degrees)	$\theta_{max} = \arcsin\left(\frac{\lambda}{2d}\right)$

Table 2.1: FMCW expressions summary

computing velocity from a single frequency ramp is not possible. However, some applications that can not operate in such a fast chirping scheme could compute velocities from long triangular frequency waveforms. The explanation behind this method is shown in figure 2.8. The delay between up-ramps and down-ramps will be different due to the fact that the Doppler frequency component adds a vertical offset. From this differences, now the range f_r and the Doppler f_d frequencies can be computed as

$$f_r = \frac{1}{2}\left(f_b(down) + f_b(up)\right) \quad f_d = \frac{1}{2}\left(f_b(down) - f_b(up)\right) \tag{2.16}$$

where f_b is the beat frequency.

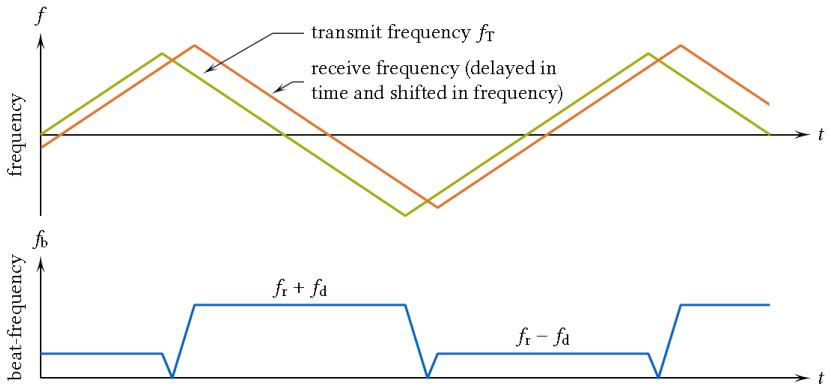

Figure 2.8: Triangular FM range and Doppler frequencies [Sia18]

Chapter 3

DemoRad evaluation board

In this chapter the DemoRad radar platform from Analog Devices is presented as the platform under test for this project. A detailed description of the main board parameters is given at the same time that some aspects of the data output and the measurement routines that can be performed, are presented.

3.1 Hardware overview

The experimental development of this project is conducted on the DemoRad evaluation board from Analog Devices. This board is an FMCW out-of-the-box radar operating at the 24 GHz band, that features two transmit and four receive antennas and includes a simple software solution for fast deployment. The providers of the internal software of the radar are INRAS, a spin-off company from the University of Linz. The module is initially designed as a demonstrative solution of radar capabilities in the 24 GHz ISM band both in range-Doppler and MIMO (massive input massive output) modes. The hardware architecture of the radar is based on the set of Analog Devices elements for automotive radar, listed below:

- Blackfin BF706 digital signal processor.
- ADF4159 PLL and ramp synthesizer.
- ADF5901 2 channel transmitter.
- ADF5904 4 channel receiver.
- ADAR7251 16 bit, 4 channel analog-to-digital converter.

The overall mode of operation of the different devices is based on the Blackfin module that is used to control the RF frontend and to process the received radar signals from the four

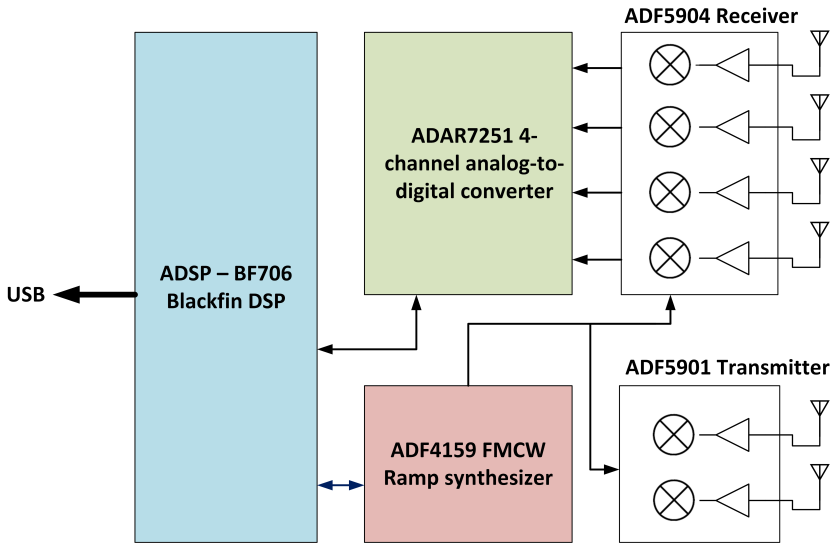

Figure 3.1: DemoRad platform signal chain

antennas. The fast waveform synthesizer (ADF4159) generates the FMCW transmit signals that are fed to the antennas via the ADF5901 two-channel transmitter. The received signals are then down-converted in the four-channel receiver (ADF5904) and the IF signals are then amplified and sampled at the ADAR7251. The board supports both real-time processing at the DSP or computer access to the data via an USB 2.0 or a CAN interface connection.

The chirp signals are generated in conjunction between the frequency synthesizer and the transmitter voltage controlled oscillator. This chirp signal is used both for transmitting and as a reference for the receiver down-conversion stage. The IF signal is sampled by the ADC and allows three different sampling frequencies: 1, 1.2 and 1.8 MSPS. As it has been presented in section 2.2.1, the sampling frequency of the ADC module is the main boundary for the maximum range of the radar. Figure 3.1 shows the interconnection between the different elements of the platform thus describing the signal chain in the RF front-end.

One important parameter of the signal chain is the transmit power. This value is an integer from 0 to 100 where the maximum output power is 8 dBm. The reference poweer-to-value relation can be found in the transmitter datasheet. In terms of chirp bandwidth, the module has a maximum operation frequency of 24.3 GHz thus enabling a maximum bandwidth of 300 MHz.

3.1.1 Physical parameters and antenna arrangement

The board is mounted on a six-layer 25 millimetre thick Rogers RO-4350 substrate. The dimensions of the printed circuit board are 100 x 100 millimetre as shown in figure 3.2. The antennas are mounted at the positions shown at table 3.1 where the central reference point is transmitter

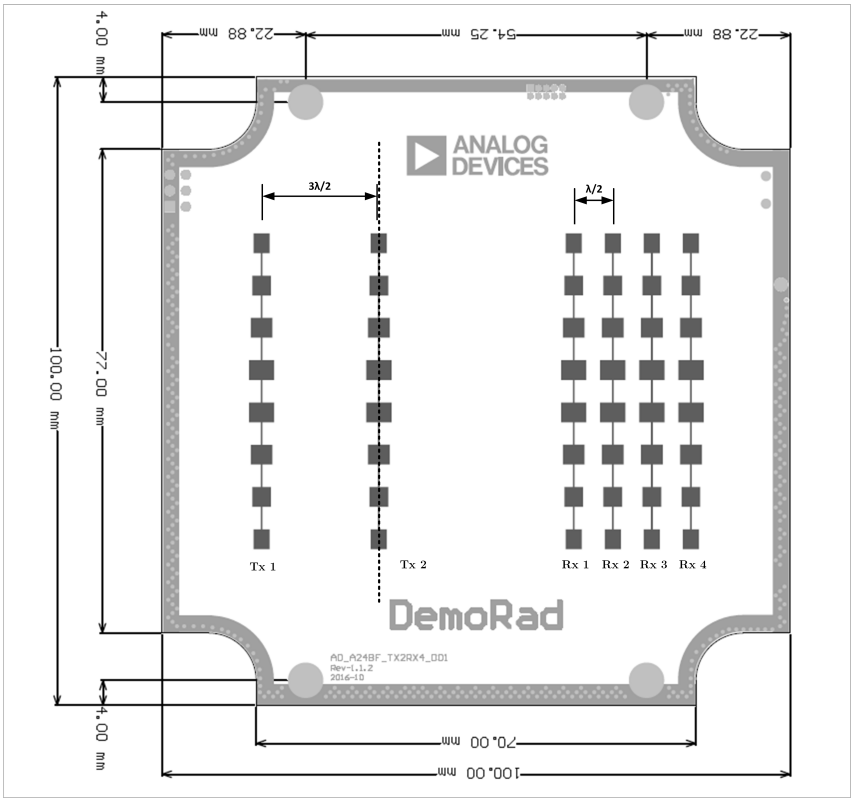

Figure 3.2: DemoRad frontside layout

two (TX2 hereinafter). See that the antenna spacing is $\lambda/2$ as was mentioned in chapter 2 and that each of them is an eight element patch antenna fed from the back of the PCB. The addition of serial elements in vertical direction tapers the beamwidth on the E-Plane (i.e. vertical) achieving a narrow vertical field of view. The horizontal field of view is therefore not affected and kept as wide as possible. Figure 3.3 is provided by INRAS [Had15] and specifies the E and H plane gain of a single 8-element antenna. The provided antenna parameters are 13.2 dBi gain, 76.5° horizontal and 12.8° vertical half power beam-width (HPBW).

In terms of energy consumption, the board needs a supply voltage of 12 Volt and a maximum supply current of 290 mA.

3.2 Firmware

Apart from the software solution by INRAS, a set of Matlab classes are provided with the board in order to allow independent radar software programming. These classes constitute the basis to control the Blackfin DSP and the different configuration parameters of the internal devices. This is done via objects from each of the classes and will be explained in the forthcoming sections. See figure 3.4 for an overview of how classes are connected.

Antenna	Horizontal position (mm)
TX 1	-18.654
TX 2	0
RX 1	32.014
RX 2	37.231
RX 3	43.449
RX 4	49.666

Table 3.1: Position of antennas on the board

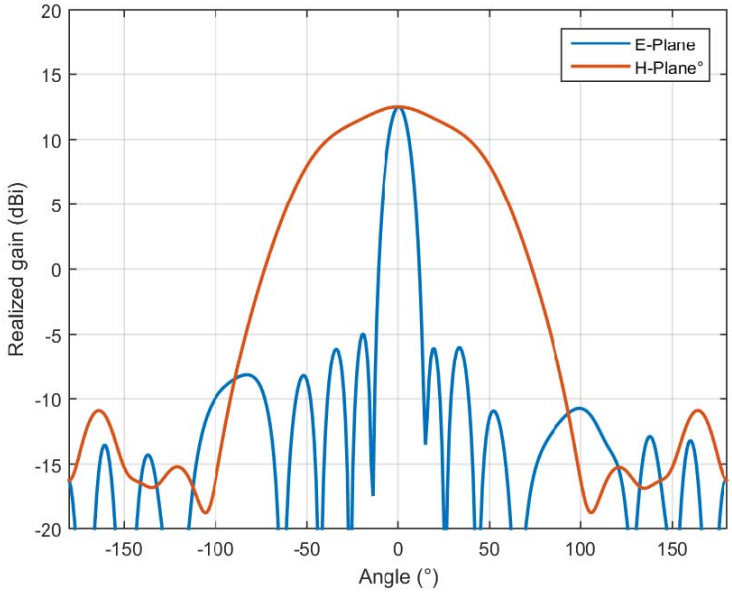

Figure 3.3: Gain of a single 8-element patch antenna

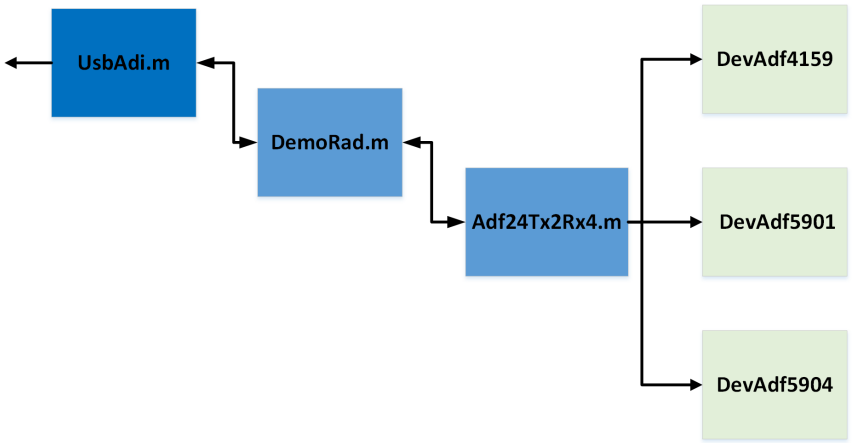

Figure 3.4: Class structure of the board

The communication between the Blackfin and the host computer works through a protected routine named *DemoRadUsb*. Therefore, the configuration steps can only be tracked until each of the orders is sent through the USB interface. The provided firmware is based on a mother Matlab class called *UsbAdi* that defines a set of functions that control direct communication with the USB interface. From this class derives the *DemoRad* class that initializes the board and defines basic parameters and functions to start and stop operation. The next step is class *Adf24Tx2Rx4*. This class defines specific operation parameters of the radar (for example, the chirp bandwidth) and contains functions concerning the initialization of the different internal devices and the configuration of the radar operation. In the end, there are three low level classes named *DevAdf4159, DevAdf5901* and *DevAdf5904* that configure internal specific parameters of the synthesizer, the transmitter and the receiver respectively. In the following subsections an straightforward outline of the classes is given in order to give a rather high-level but complete description of the firmware structure.

3.2.1 UsbAdi

Class *UsbAdi* is the *handle* class that serves information directly to the USB interface defined by the *DemoRadUsb* Mex file. Inside the class, three public properties are defined: UsbOpen, UsbDrvVers and stUsbAdiVers. UsbOpen stores the actual status of the connection with the board and the two Vers properties are fixed values related to the code version. The actual version of the USB interface is 1.1.0.

The class defines a set of key functions in terms of communication with the board: *CmdBuild*, *CmdExec*, *CmdReadData*, *CmdRecv*, *CmdSend*, *DataRead* and *Data Send*. These functions give the specific format to the information that is transferred to the board and also give orders to the board in order to read content from its memory. The bus width of the DSP module is 32 bit and thus all read/write orders have to be translated into a 32 bit-long word containing both operation codes and memory addresses.

3.2.2 DemoRad

The *Demorad.m* class is the initialization of the DemoRad board and its parent superclass is *UsbAdi*. In the properties section, the following parameters are defined:

- *DebugInf* is a boolean parameter that enables the display of messages as a debugging tool, while the radar operates.
- *stBlkSize, stChnBlkSize, ChirpSize, CalPage, Rad_MaskChn, Rad_NrChn* and *stDemoRadVers* are numerical definitions of the size of the internal strings that need to be handled by the DSP. These are parameters that refer to register sizes and low-level data handling.

- $Rad\_N = 256$ is a very important parameter that defines the amount of samples that the ADC takes from each of the IF tones (i.e. from each of the chirps). This value is fixed in the current framework because of the ADC behaviour, and it will be discussed later on. A deeper study on the hardware architecture of the board would enable the modification of this parameters but falls out of scope in this project.

- $FuSca = 0.498/2^{16}$. FuSca stands for Full Scale and encodes the Full Scale Range of the ADC. This range means the maximum Vpp value that the ADC can handle within its quantification range and is divided by amount of values the converter can quantize. The ADAR7251 module has several operation modes but the one selected in this board is $G_{ADC} = 21.98\ dB$ and thus maximum voltage range is 0.498 Vpp[1], which divided by 2^{16} yields the voltage value of the least significant bit (LSB). This variable is of key importance as it allows accurate mapping of FFT values to voltage.

- *ADR7251Cfg, ADIFMCWCfg, ADICal* and *ADICalGet* are arrays composed of 32 bit long configuration words for different devices on the board. For example, ADR7251Cfg contains the whole register configuration of the ADC in order to set it ready for operation. From each of the 32 bit words, the 16 most significant bits are the register address and the 16 least significant bits are the data to be stored into the registers.

The class also defines a long list of methods but only those strongly related with the project are detailed. The ones that are not explained concern actions such as displaying the board or the DSP status, setting up the SPI configuration or reading information from the EEPROM memory, among others.

- *BrdGetChirp* is a key function in the radar setup. This function commands the module to send, sample and return the data from a set of chirp signals. The length of the chirp frame is defined by parameters StrtPos and StopPos.

```
function    Ret     =   BrdGetChirp(obj, StrtPosn, StopPosn)
StopPosn        =   obj.InLim(StopPosn, 1, 128);
StrtPosn        =   obj.InLim(StrtPosn, 0, StopPosn - 1);
DspCmd          =   zeros(3,1);
Cod             =   hex2dec('7003');
DspCmd(1)       =   1;
DspCmd(2)       =   StrtPosn;
DspCmd(3)       =   StopPosn;
Ret             =   obj.CmdReadData(0, Cod, DspCmd);
Ret             =   Ret(:,end:-1:1);
```

StopPosn and StrtPosn are bounded between 0 and 128, being 128 the maximum chirp-frame length. This limitation comes from the physical limitation of the DSP internal

[1]See Analog Devices data sheets on these modules for a detailed explanation of the different modes of operation.

memory and the need of transferring it to the computer after taking the measurement. Note that the last step in this function is a backwards reorder of the chirps that are output so that the output array is FIFO structured (the first emitted chirp is at the first position). The code above is given as an example of how do functions in this module look like. The procedure is similar in almost every method involving communication from the computer to the board and consists on building an array containing the command parameters (Cmd) and the operation code that has been fixed inside the encrypted Mex file. In the end, every communication step uses one of the functions defined in the *UsbAdi* class.

- *BrdGetCalDat* and *BrdGetCalInf* are two methods that return the calibration data stored in the EEPROM memory of the DSP. This data is used to allow MIMO angular estimation, and can be re-written if a new calibration is performed.

- *Dsp_SetMimo* enables the MIMO mode of the module. This mode consists on alternating TX 1 and TX 2 for each chirp.

- *BrdRst* resets the board to its default status. It is required to reset the internal registers after each measurement in order to load different configuration parameters.

3.2.3 Adf24Tx2Rx4

Class *Adf24Tx2Rx4* is the child class of *DemoRad* and apart from all the inherited content, it defines three public sub-objects named *Adf_Rx*, *Adf_Tx* and *Adf_Pll*. As private properties, this class specifies default configuration parameters that are needed to initialize the board when it is powered up, although they are reconfigured before each measurement routine. Some of this parameters for example are $Rf\_fStrt = 24e9$ or $Rf\_fStop = 24.25e9$.

- Constructor *Adf24Tx2Rx4* creates 3 objects inside the *Adf24Tx2Rx4* object, each one concerning the configuration of the receiver (ADF5904), the transmitter (ADF5901) and the synthesizer (ADF4159).

- *RfRxEna* enables and powers up the selected channels of the receiver. In normal operation condition, the four channels are powered up.

- *RfAdf5904Ini* and *RfAdf4159Ini* are functions that initialise each of the objects of the receiver, transmitter and synthesizer. The initialization of each object is defined inside the corresponding class but in general terms, it consists on generating all the values that need to be loaded in the device registers.

- *RfTxEna* is the initialization function of the transmitter chip. The input parameters are the transmission channel (TxChn) and transmission power (TxPwr).

- *BrdGetData* is the measurement trigger function. By calling *BrdGetData*, function *BrdGetChirp* from class *DemoRad* is used.

```
function    Ret     =   BrdGetData(obj)
Ret     =   BrdGetChirp(obj, obj.StrtIdx, obj.StopIdx);
end
```

  See that *BrdGetChirp* is called stating StrtIdx and StopIdx. These parameters will be explained in detail in section 3.3.

- *RfMeas* is a function that requires a more detailed explanation to understand how the DemoRad board works. The code of this function is the following:

```
function    ErrCod      =   RfMeas(obj, varargin)
ErrCod      =   0;
if nargin > 2
 stMod       =   varargin{1};

 if stMod == 'Adi'
 disp('Simple Measurement Mode: Analog Devices')
 Cfg             =   varargin{2};

  if ~isfield(Cfg, 'fStrt')
   disp('RfMeas: fStrt not specified!')
   ErrCod      =   -1;
  end
  if ~isfield(Cfg, 'fStop')
   disp('RfMeas: fStop not specified!')
   ErrCod      =   -1;
  end
  if ~isfield(Cfg, 'TRampUp')
   disp('RfMeas: TRampUp not specified!')
   ErrCod      =   -1;
  end

  if isfield(Cfg, 'StrtIdx')
   obj.StrtIdx    =   Cfg.StrtIdx;
  end
  if isfield(Cfg, 'StopIdx')
   obj.StopIdx    =   Cfg.StopIdx;
  end

  fsSel                   =   [1, 1.2, 1.8].*1e6;
  if isfield(Cfg, 'fs')
   [Val ClkSel]        =   min(abs(fsSel - Cfg.fs));
   ClkInt              =   1/fsSel(ClkSel);
  else
   ClkSel              =   1;
```

```
    ClkInt              =   1e-6;
   end

  %Eloi: the following 2 if loops, check if TRampUp time
  %is less than 260 samples in the new sampling frequency
  %(and TrampDo is less than 10)

   if obj.Rf_TRampUp/ClkInt < 260
    warning('Adf24Tx2Rx4: Set TRampUp to 260 clock cycles')
    Cfg.TRampUp     =   260*ClkInt;
   end

   if obj.Rf_TRampDo/ClkInt < 10
    warning('Adf24Tx2Rx4: Set TRampDo to 10 cycles')
    Cfg.TRampDo     =   10*ClkInt;
   end

  switch(ClkSel)
  case 1 %Sampling freq 1 MHz
   obj.ADR7251Cfg(7)   =   hex2dec('00010000') + 100;  %M
   obj.ADR7251Cfg(8)   =   hex2dec('00020000') + 76;   %N
   obj.ADR7251Cfg(9)   =   hex2dec('00032833'); %PLL Control
   obj.ADR7251Cfg(10)  =   hex2dec('01400000') + 3;
   Cfg.Tp   =    ceil(Cfg.Tp/1e-6)*1e-6;
   Cfg.TRampUp   =    ceil(Cfg.TRampUp/1e-6)*1e-6;

  case 2 %Sampling freq 1.2 MHz
   obj.ADR7251Cfg(7)   =   hex2dec('00010000') + 1000;
   obj.ADR7251Cfg(8)   =   hex2dec('00020000') + 304;
   obj.ADR7251Cfg(9)   =   hex2dec('00031003');
   obj.ADR7251Cfg(10)  =   hex2dec('01400000') + 3;
   Cfg.Tp   =    ceil(Cfg.Tp/5e-6)*5e-6;
   Cfg.TRampUp   =    ceil(Cfg.TRampUp/5e-6)*5e-6   ;

  case 3 %Sampling freq 1.8 MHz
   obj.ADR7251Cfg(7)   =   hex2dec('00010000') + 1000;
   obj.ADR7251Cfg(8)   =   hex2dec('00020000') + 304;
   obj.ADR7251Cfg(9)   =   hex2dec('00031003');
   obj.ADR7251Cfg(10)  =   hex2dec('01400000') + 2;
   Cfg.Tp   =    ceil(Cfg.Tp/5e-6)*5e-6;
   Cfg.TRampUp   =    ceil(Cfg.TRampUp/5e-6)*5e-6;
   otherwise
  end

  Cfg.ClkInt                  =   ClkInt;
  Cfg.ClkSel                  =   ClkSel;
```

```
    obj.Rf_fStrt                =   Cfg.fStrt;
    obj.Rf_fStop                =   Cfg.fStop;
85  obj.Rf_TRampUp              =   Cfg.TRampUp;
    obj.Rf_TRampDo              =   Cfg.Tp - Cfg.TRampUp;
    Cfg.TRampDo                 =   Cfg.Tp - Cfg.TRampUp;

    disp(['Sampling frequency: ', num2str...
90   (fsSel(ClkSel)/1e6), ' MSPS'])
    obj.ADIFMCWCfg(9)       =   ClkSel;

    % Eloi: Configure ticks which are ignored in sampling
    Ticks               =   floor((Cfg.TRampUp + ...
95   Cfg.TRampDo)/ClkInt);
    obj.ADIFMCWCfg(8)   =   Ticks   - 256 - 1 - 7;

     %Eloi: The following command applies ADI7251Cfg and
     %ADIFMCWCfg to the ADAR ADC module.
100 obj.Dsp_SetAdiDefaultConf();

    if isfield(Cfg, 'MimoEna')
     if Cfg.MimoEna > 0
      obj.Dsp_SetMimo(1);
105  end
    end

    obj.RfAdf4159Ini(Cfg);

110 ErrCod = Cfg;
      end
     end
    end
```

RfMeas is responsible for setting up the main parameters of the chirp signal that are fixed by the user in the measurement routine. These parameters are *TRampUp, TRampDo, Rf_fStrt, Rf_fStop, fs, Tp, StrtIdx and StopIdx*, that stand for the chirp up-ramp and down-ramp time, the initial and end frequency of the ramp, the sampling frequency, the total duration of a chirp and the indices of measurements, respectively. Before loading the configuration to the registers, the completeness of the values is revised. At first, all parameters are double-checked and loaded into the *Cfg* struct that will be passed to the initialization functions. One interesting parameter to understand is *fs* or the sampling frequency. As stated in section 3.1, three sampling frequencies are possible: 1, 1.2 and 1.8 MSPS. So, whichever value is entered in the sampling frequency parameter in the measurement value, it will be rounded down to the nearest allowed frequency (see code line 30). After selecting the clock of the system, the function checks if the desired *TRampUp* at

that sampling frequency would yield 260 samples or more. If not, the ramp-up is modified to the minimum value that yields at least 260 samples. At the same time, selecting the sampling frequency involves changing some of the configuration parameters of the ADC module and therefore, the "switch case" structure is needed. Note that ramp-up time and chirp duration (up-ramp and down-ramp) are rounded so that they are integer valued (code line 59 and 60). Another interesting parameter to take into account is the *Ticks* variable. Due to the synthesizer response, the chirp ramp is not ideal. There exists some ripple in the beginning of the ramp and also some down-ramp time is needed to let the PLL restart. Because of this, the *Ticks* value defines how many samples from the total ones taken of the IF tone, need to be discarded, because they are not correct. As said before, the maximum amount of samples per chirp is bounded to 256 because it is the optimal power of two value for the given sampling frequencies and the maximum sweep bandwidth of 300 MHz.

3.2.4 Device classes: DevAdf4159, DevAdf5901 and DevAdf5904

A thorough explanation of the classes themselves falls out of scope in this project as the configuration of them is low-level. Understanding all the modified parameters would require a deep analysis of the data sheet of each device. In general words, each of the devices has a set of internal registers where different values need to be loaded. For example, the emission power of the transmitter or the low noise amplifier (LNA) gain at the beginning of the receiver signal chain. Inside the classes, a detailed map of all the inner registers of each device is given. The different functions are designed to translate the predefined configuration into 16 bit-long words including masks and register addresses.

3.3 Measurement software

The explanation of the internal components of the radar platform in the previous section is necessary in order to fully understand the measurement routines presented at this point. Firstly, it is interesting to present the hardware constraints that explain the measurement behaviour of the platform under test; in this case, the chirp frame length needs to be considered. To clarify nomenclature as in 2.2.2, a chirp frame is a set of chirps that are emitted one after the other and that are sampled continuously. Thus, the only unused periods that need to be considered are both the synthesizer idle times at the beginning and the down-ramp periods in the end of each chirp. These periods are considered in the *ticks* variable defined in class *Adf24Tx2Rx4*. Due to memory handling limitations and the need to perform calculations (i.e. FFT) on the data, the frame length in this platform is bounded to 128 chirps. This is an important figure to consider, as it means that the longest block of coherent data will be 128 times the duration of a

chirp. With this, two different measurements will be defined: the 128 chirps frame and the single chirp measurements. This last approach can also be called the "receive and save" measurement because only one chirp is transmitted, sampled and stored. In a single chirp measurement, there will not be coherence between the chirps, but will be of use in terms of characterizing the behaviour of the platform.

3.3.1 Chirp parameters

Once the meaning of a frame is clear, the key parameters of the chirp signal need to be considered. They have been slightly presented in the previous section and are now stated in table 3.2.

Parameter	**Value**	**Definition**
TxPwr	0 - 100	Transmission power. Integer value from 0 - 100.
fs	1e6, 1.2e6 or 1.8e6	Sampling frequency
fStrt	24e9	Start frequency (min. 23.95 GHz)
fStop	24.3e9	Stop frequency (max. 24.3 GHz)
TRampUp	260/fs	260 samples at either sampling frequency
Tp	300/fs	300 total samples at either sampling frequency
N	256	Effective samples per chirp (fixed)
StrtIdx	0	Starting point of the chirp frame
MimoEna	boolean	Enables MIMO mode
StopIdx	1 - 128	Last chirp to be recorded
TxAntenna	1 - 2	Tx1 or Tx2
NumFrames	1 - inf.	Amount of frames to be recorded in a loop

Table 3.2: Main chirp parameters

Note that the chirp bandwidth can be defined as $B_{chirp} = fStop - fStrt = 300\ MHz$ (in this case the maximum available frequency sweep is used) and that $NumChirps = StopIdx - StrtIdx$. From the *RfMeas* function presented in section 3.2.3 it can be seen that the parameters mentioned above, that are needed to initialise the platform, are passed to the function using a *struct*. Therefore, in the measurement routine the variable *Cfg* is defined containing all of them but *TxPwr, NumFrames* and *TxAntenna*, that are not used in the *RfMeas* function.

3.3.2 Board control

The parameters of the chirp have been defined so now the board needs to be initialised to measure. The first step is to create an object of the *Adf24Tx2Rx4* class and reset the board so as to ensure that there are no pre-charged values in the registers. After that, functions *RfRxEna* and *RfTxEna* are called to power-up the receivers and the selected transmitter.

```
Brd = Adf24Tx2Rx4();
Brd.BrdRst();
Brd.RfRxEna();
Brd.RfTxEna(TxAntenna, TxPwr);
Config = Brd.RfMeas('Adi', Cfg);
```

3.3.3 Data Output

Once the board is ready to measure, the *BrdGetData* function can be called and the data of a measurement will be saved into the destination variable. This function will output a 256×4 matrix when the length of the frame is one and a $128 \cdot 256 \times 4$ matrix if the frame length is 128. Here each row is a time instant (i.e the first 256 rows are the 256 samples of one chirp) and each column is one of the four different receiver channels. In figure 3.5 the output of a single chirp measurement is plotted. See that it is the time-domain representation of the IF tone explained in the theory chapter.

If more than one frame is to be stored, a measure loop is needed. However, the matrix where the output data is loaded after calling *BrdGetData* is overwritten at each iteration. This can be solved by means of concatenating the output data after each iteration, for example. In this project, the standard data format has been defined as a $256 \times NumChirps$ matrix for each of the channels. The following code is an example of how data can be stored in an overall matrix *DataOut* that contains a set of single chirp measures.

```
for Idx = 0:NumFrames-1
     Data      =    Brd.BrdGetData();
     DO_row = Idx*256;
     DataOut(DO_row+1:DO_row+256, :)    =    Data;
end
```

3.4 Module capabilities

In the previous section the chirp parameters have been introduced and it has been shown that some of them are bounded because of hardware limitations. Now, it is possible to asses the

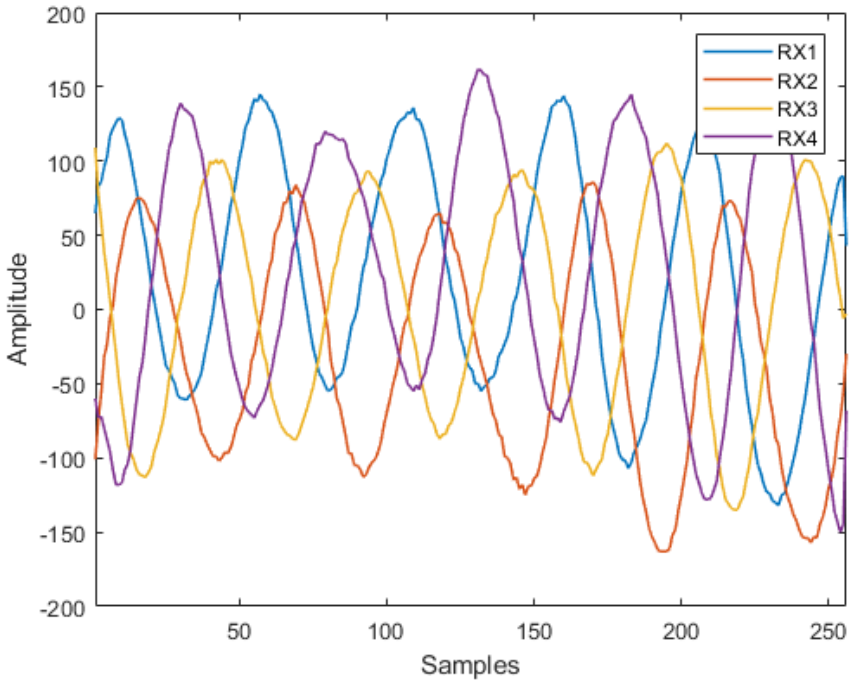

Figure 3.5: Time-domain representation of a sampled IF tone

theoretical performance that the radar platform yields in any of the three radar observables: range, velocity and angle of arrival.

As presented in section 2.2.1, the range resolution is limited by the chirp bandwidth and the maximum range is basically bounded by the sampling frequency. Therefore, using equations presented in chapter 2, the results shown in table 3.3 are obtained.

Key figure	**Theoretical value**
Range resolution ΔR (m)	0.5
Maximum range R_{max} (m)	65 (at 1 MSPS)
Velocity resolution Δv (m/s)	0.1628
Maximum velocity v_{max} (m/s)	10.41
Angular resolution (at 0°) (degrees)	28.64

Table 3.3: *DemoRad* capabilities

In the following chapters of this project, the actual performance capabilities of the radar platform will be tested and proved.

Chapter 4

Experimental set-up

This chapter presents the experimental set-up and different steps that have been followed to assess the performance of the platform. The scattering phenomenon has been introduced in chapter 2 and it is the reason why testing a radar sensor is not a simple experiment. The fact that electromagnetic waves will be reflected by almost every surrounding object forces the use of a completely controlled environment where well known targets are used. In this project the experiments are carried out in an radio-frequency anechoic chamber and the need of a characterized target to study, is solved with the design of a corner reflector.

4.1 Trihedral corner reflector

Since the beginning of radar technology the trihedral corner reflector has been the most used target because it fulfils the requirement for accurate radar calibration: a known RCS behaviour. The trihedral reflector is based on the well-known case of a conductor corner at which an electromagnetic wave impinges. The presence of a 90° angle and the fact that the material is conductor causes the wave to be backscattered in the same direction of incidence. Therefore, the reflector yields a strong echo signal.

Different reflector shapes are available depending on the application. For example, the most used configuration in maritime radar is the octahedral reflector, which forms a sphere with one corner at each of the quadrants, or in the aeronautics field, the dihedral formation at the tail of a plane allows aircraft detection. In the case of this project the selected shape is the trihedral one. This type of reflector, shown in figure 4.1, is based on a cut-out of a cube of edge length l. The cut yields a corner with three equal-sized triangular faces that ensure the same azimuthal field of view for a wide range of elevation angles.

See that the length of the inner sides is l and thus the outer sides must be $\sqrt{2}l$. If these

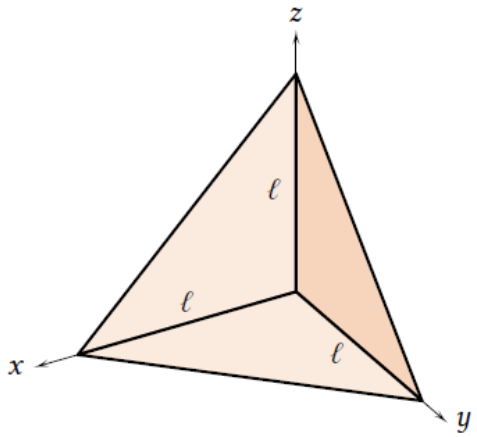

Figure 4.1: Trihedral reflector ideal model and dimensions [Sia18]

dimensions are met, the radar cross section of such construction can be calculated as in (4.1). The selected edge length is found to be 77.2 millimetres to obtain an RCS of 1 m^2 at 24 GHz. Such an RCS is the one associated to a human-being. Additionally, to attach the corner reflector to a tripod or a pedestal and take measurements, it is important to correctly face the corner to the radar and thus an inclination of 35.26 degrees[1] is needed.

$$\sigma = \frac{4\pi l^4}{3\lambda^3} \tag{4.1}$$

The design of the reflector has been carried out using FEKO in order to simulate the RCS response of the configuration before building it. Figure 4.2a shows the simulated monostatic RCS of the reflector and Fig. 4.3 shows the graphical representation of the bistatic RCS at a frequency of 24.125 GHz. As explained in 2, the monostatic RCS is the backscattered power received at the same position at which it was emitted, and the bistatic RCS represents how the power is scattered in every direction for one single incident angle. See that, a peak of almost 0 dBm^2 is reached at $\phi = 0°$ and that secondary peaks at 40 and -40 degrees correspond to positions where due to orientation, both a portion of the internal cavity and the outer side of the reflector are illuminated by the radiating source. Although the reflector is made of a conductor material, the field distribution behind the corner reflector appears due to diffraction on the edges of the aperture. This diffraction phenomenon is something to consider if an optimal RCS is to be achieved. Additionally, the RCS of the model has been simulated in the range from 20 to 30 GHz to approach the variations in terms of frequency. The cross section of the reflector increases linearly with frequency at the same time that it oscillates because at this frequency lapse, the reflector is in the Mie resonance region (see figure 4.2b).

[1]This angle derives from the vertical orientation of a right triangle having leg size of 1. $acos(\sqrt{2}/\sqrt{3}) = 35.26°$

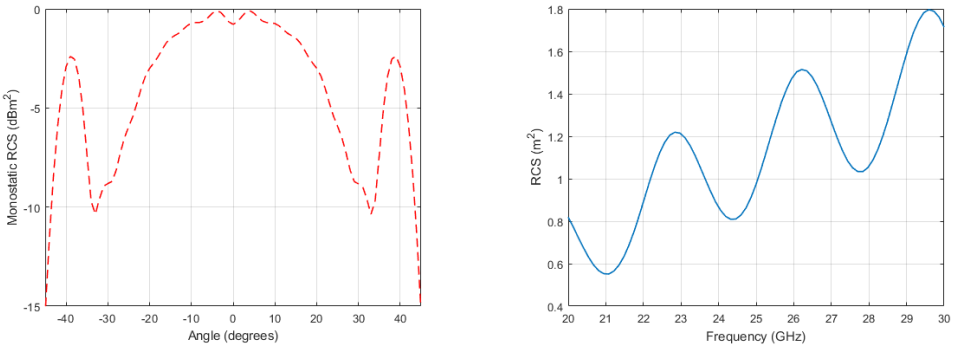

(a) Monostatic RCS at 24 GHz (b) Monostatic RCS from 20 to 30 GHz

Figure 4.2: RCS of the corner reflector

After design and simulation, the reflector has been built and the actual result is shown in picture 4.4. The model is built in a solid aluminium cube and the trihedral structure is milled. Adding screw holes to the bottom of the reflector is necessary to attach it to an specific mount pad or a tripod.

4.2 Anechoic chamber

Now that the problem of finding a target is solved, the focus falls on recreating a controlled environment in which measures can be made accurately and in which there is no doubt that the detected target is the corner reflector. In this case the chosen environment is the electromagnetic anechoic chamber at the Telecommunication Systems department at UAB. This chamber is designed to provide RF isolation for a range of frequencies from 400 MHz to 6 GHz and the conductive foam absorbers provide absorption of 50 dB from 10 MHz to 18 GHz [MVG16]. However, a certain degree of absorption is also present at 24 GHz as no reflections were observed by the radar in the initial tests. The chamber contains two motorized pedestals that are precisely aligned and that have different movement capabilities: the DUT (Device Under Test) pedestal can rotate both in azimuth and in polar orientation and the probe pedestal only rotates in polar direction. Following this considerations the radar is mounted on the DUT and the corner reflector is attached to the probe. Each pedestal has a metallic circular mount at which antennas are tied in the common measurement set-up. In this case, in order to tie de radar and the reflector to their respective pedestals, a PVC plate is used as base and thus a vertical offset with respect to the rotation axis has to be considered. The radar module and the target have a vertical offset of 10.5 and 12 centimetres respectively and in the end, the distance between the module and the radar is measured to 2.55 meters. In pictures 4.5a and 4.5b the experimental set-up inside the chamber is shown. The objective of this configuration is to accurately measure controlled orientation angles to prove the radar range and angular estimation capabilities.

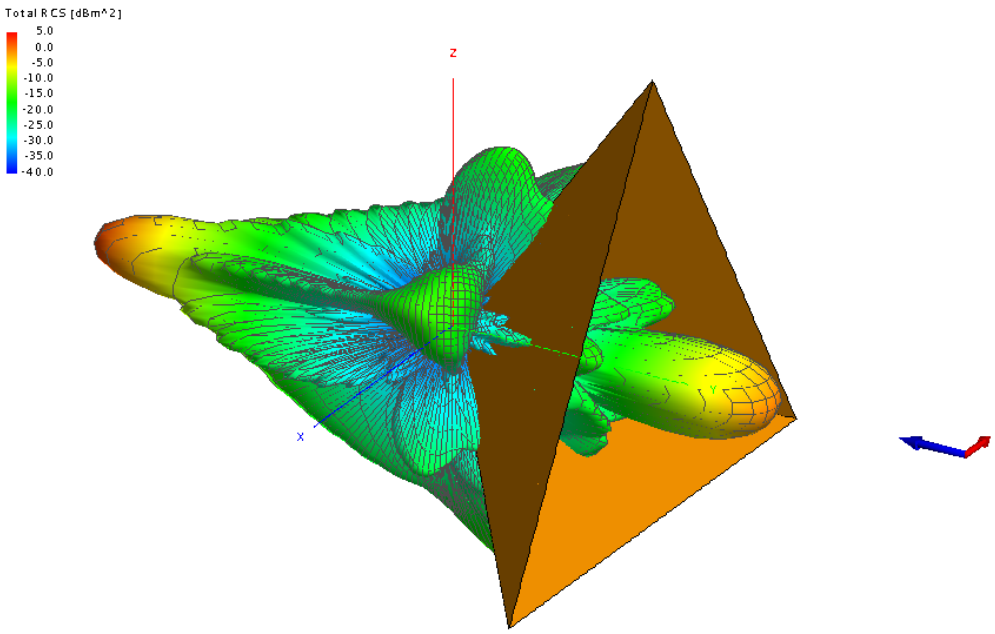

Figure 4.3: 3D representation of bistatic RCS

However, the pedestals in the chamber can not be automatically moved in range direction and there is no possibility to simulate velocity measurements with the reflector.

4.3 Measurements and analysis

In the defined environment, it is now time to start taking measurements. First of all, it is important to define which type of measures are of interest to extract information. In this case, three different routines have been performed in the chamber each consisting in one of the different measurement procedures the platform supports. The first one is a single-chirp measurement of 400 chirps at angles spanning from -45 to 45 degrees with steps of 15 with two results per orientation: one per transmitter. The second measurement is a frame of chirps from -75 to 75 degrees with steps of 3, also using TX 1 and TX2, and the third one is another time a frame of chirps from -75 to 75 with steps of 3 but now using the MIMO mode, that means to transmit alternating the transmitters. The signal parameters in use during measures are specified in the following table. Note that both the transmit power and the swept bandwidth are set at their maximum levels in this cases. Additionally, to study the effect of the bandwidth on range, an extra single-chirp measurement at 0° using different bandwidths is also recorded.

See that the simulation of different arrival angles is achieved by rotating the radar and in the anechoic chamber, the angular direction is defined in a DUT-centred coordinate frame.

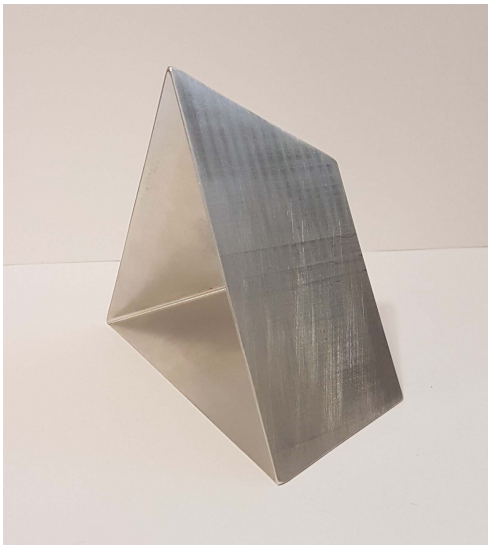

Figure 4.4: Aluminium corner reflector prototype

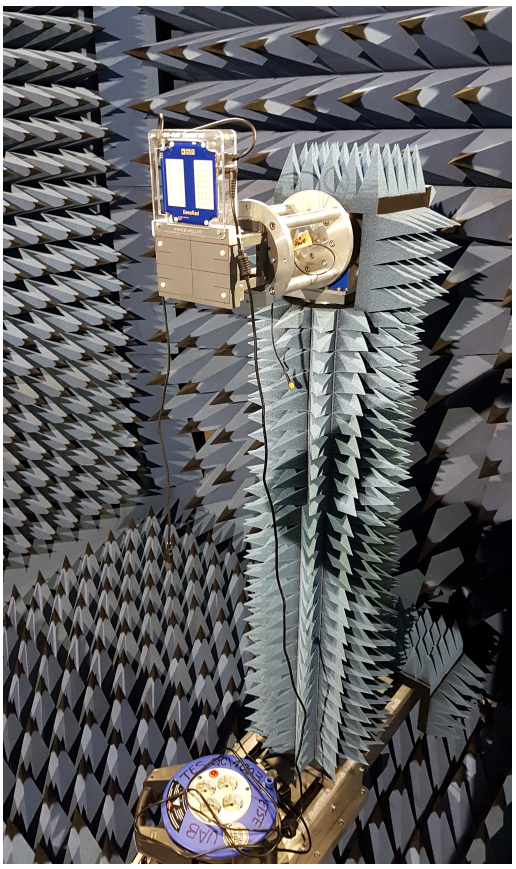

(a) Sideview of the radar module

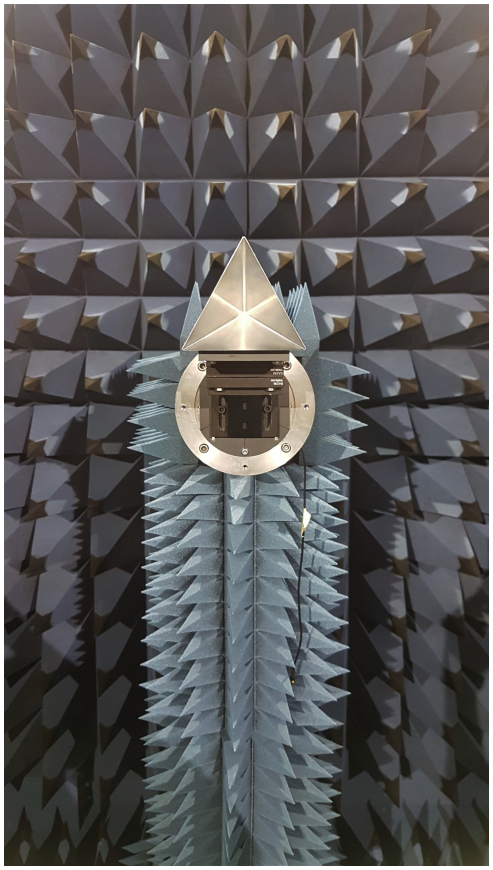

(b) Front view of the reflector

Figure 4.5: Experimental set-up in the anechoic chamber

Parameter	Value
TxPwr	100
fs	1e6
fStrt	24e9
fStop	24.3e9
TRampUp	260/fs
Tp	300/fs

Table 4.1: Measurement signal configuration

When both pedestals are facing each other the angle is considered to be 0° and when the moving pedestal is rotated to look to the left-hand side, the angle is considered negative. Therefore, when the radar is rotated to a negative angular position, the situation is equivalent (from the radar point of view) to a target at a positive angle of incidence.

4.3.1 Range profile and resolution

The first analysis of the platform is performed on the range profile computation and the data that has been used in this analysis are the measures corresponding to 400 single chirps at an angle of arrival of 0 degrees. As mentioned in section 3.3.3, the data output format that has been configured is a 256×400 matrix for each of the channels where each of the columns is the set of 256 samples of the IF tone from a single chirp. To compute the range profile, the first step is to perform a Fast Fourier Transform along dimension 1 of the channel matrix[2]. In the following code line, the specific call is explained.

```
range_profiles.Chn1 = ...
fftshift(fft(measures.Chn1(:,:).*Win2D_long ,NFFT,1),1).*FuSca/ScaWin;
```

- The amount of range bins for the FFT is `NFFT` = 4096. This value is the one usually applied in FFT on frequencies up to 1 MHz. For 4096 bins, 2048 will correspond to the positive side of the spectrum and therefore, the range of 0 to 65 meters will be mapped into 2048 different values, yielding a *bin resolution* of 0.031 metres per bin. See that this *bin resolution* is an effect of the `NFFT` value and affects the accuracy of the result because it defines the range mapping axis. The actual range resolution presented in previous sections is defined from the waveform characteristics.

[2]First dimension means along column in Matlab.

- *Win2D* is a 256-sample Hann window (also known as Hanning) that is applied to the time domain samples to scale the output of the FFT. Hann windows are commonly used in Fourier transformation to reduce the level of the side lobe of the windowing *sinc* function. In exchange for side lobe reduction, the width of the main lobe increases, thus loosing resolution. After applying the FFT, the output is rescaled with `ScaWin`, that is the sum of the whole Hann window, and also the parameter `FuSca` (Full Scale) is applied so that the output is voltage valued.

- Note that both `fft` and `fftshift` are applied in dimension 1 (to each column). If not specified, the transform would be applied to the whole matrix in two dimensions.

The value that is saved as the output of the FFT is a 4096 element array that contains both sides of the spectrum of the sampled IF signal. Theoretically, this spectrum does have a maximum at the exact frequency that maps to the distance at which the target is located. In order to plot the profile, the distance axis has to be approached recalling equation 2.5. The distance values can then be computed using the following code line, where the IF values are the ones comprised by the range bins times the sampling frequency, and the chirp slope is the swept bandwidth divided by the ramp-up time.

```
range_freqaxis = [-NFFT/2:NFFT/2-1].'./NFFT.*fs.*c0/(2.*Chirp_slope);
```

Applying the mentioned computations, the results obtained at an angle of arrival of zero degrees are shown in figure 4.6. Figure 4.6a shows the averaged range profile (along the 400 single-chirp set) obtained by each of the receivers using TX1, and 4.6b shows TX2. The green line on the figures is the reference power decay expected from a 0 dBm^2 target using Friis transmission formula (2.2)[3], as follows:

$$P_R = P_T + 2\ G_{TX} + 20\ log\left(\frac{\lambda}{r^2}\right) + 30\ log\left(\frac{1}{(4\pi)}\right) - 13 + 10\ log\left(\sigma_{lin}\right) \tag{4.2}$$

where $G_{TX} = 13.2\ dBi$, $\sigma_{lin} = 0\ m^2$ and $P_T = 8\ dBm$[4].

Results do match the calculated reference line achieving a target localization of 2.571 meters for both transmitters and a received power of $-67.9\ dBV$ for TX1 and $-65.9\ dBV$ for TX2. Note that high distance-measurement accuracy is achieved and that there is a slight difference in received power for each of the transmitters. At the same time, see that there is a power peak resolved at 0 meters that decays fast. This peak corresponds to an initial mutual coupling maxima between the transmit and the receive antennas of the module; in the radar field it is usually know as the *blind distance*. The use of transmitter two yields higher mutual coupling

[3]Factor -13 converts from dBm to dBV.

[4]`Tx_Pwr` is set to 100.

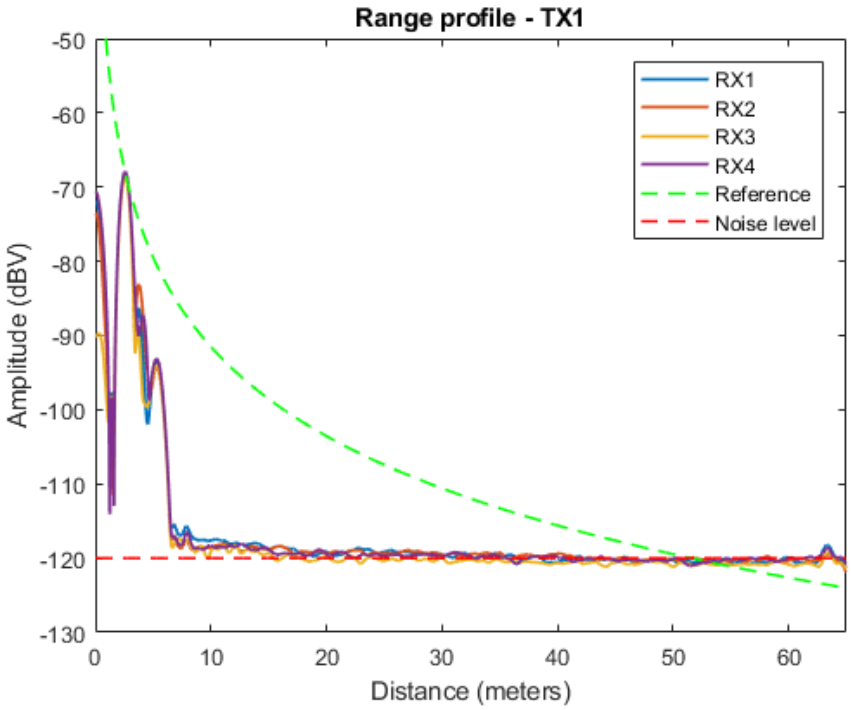

(a) Range profiles using TX 1

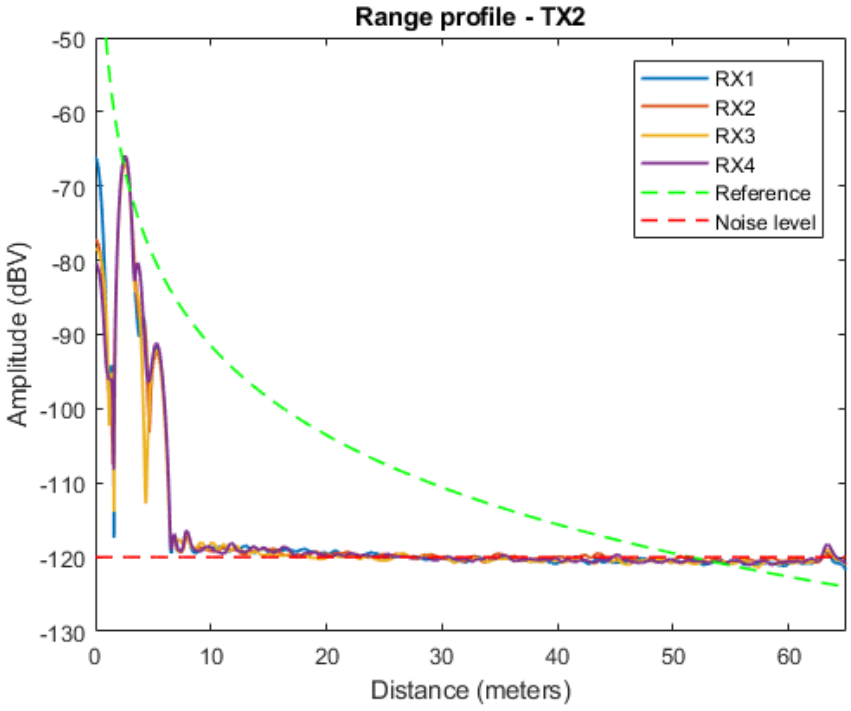

(b) Range profiles using TX 2

Figure 4.6: 400 single-chirp averaged range profile at each RX channel

with RX1 (blue line in figure 4.6b) if compared to the coupling with the other receiving antennas. This is understandable as TX2 and RX1 are spaced only $3\lambda/2$ (see figure 3.2), being the closest transmitter-receiver distribution in the radar platform. Furthermore, the mentioned difference in received power is also caused by the higher coupling of TX 2.

Amplitude stability

As a second analysis, an important feature to test on all type of sensors is the repeatability and stability of results. Therefore, it is interesting to look at the behaviour of the amplitude of the maximum at which the reflector is resolved. To do this, the maximum amplitude is found to be bin 82 of the positive side of the spectrum and in figure 4.7 the amplitude values at each channel along the 400 single-chirps are shown. See that the amplitude is stable within chirps which ensures that results are repeatable for non coherent chirps.

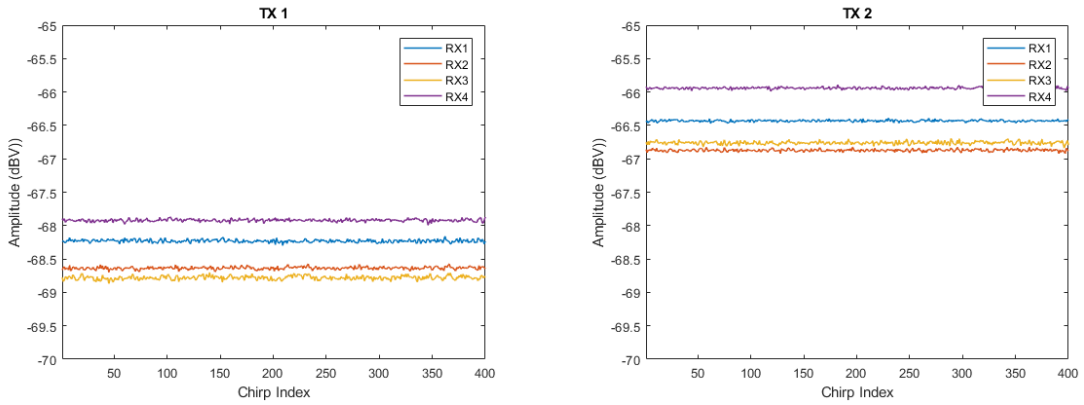

(a) Stability using TX 1

(b) Stability using TX 2

Figure 4.7: Bin 82 amplitude of 400 single-chirp measure (DoA = 0°)

In a single-chirp measurement the idle time between chirps is long enough for the RF front-end to return to the initial stable state before emitting the next chirp. However, in a more realistic environment where chirp frames are the operation mode, it is important to check that the amplitude of the selected bin in a frame is as stable as in a single-chirp case. The position of the reflector is another time resolved at the 82nd bin, proving that the range computation does not change depending on the operation mode, and figure 4.8 shows the results for the amplitude stability on a frame. Thus, the RF front-end is stable in terms of amplitude also in a frame of chirps. The variations that can be observed in the figures are due to the noise that is added to the signal, in the RF front-end.

Range resolution and swept bandwidth

One of the parameters that can be altered when configuring a measurement routine, is the swept bandwidth. The measures in the previous paragraphs have been performed using the

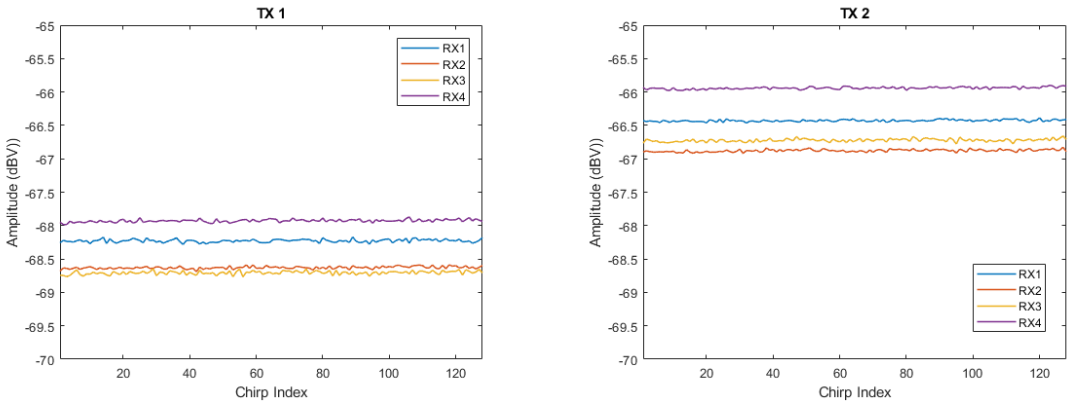

(a) Stability using TX 1

(b) Stability using TX 2

Figure 4.8: Bin 82 amplitude of a chirp frame measure (DoA = 0°)

maximum available bandwidth of the synthesizer, that is 300 MHz. However, it would also be interesting to characterise how does the swept bandwidth affect range computation performance in the DemoRad platform. To do so, a single-chirp measurement at an angle of 0° has been taken for a set of 200 chirps at 6 different swept bandwidths: 50, 100, 150, 200, 250 and 300 MHz. In fact, as T_{sweep} is kept at 260 μs, the parameter that is altered is the chirp slope, commonly referred as $\mu = B/T_{sweep}$. Figure 4.9 shows the position at which the corner reflector is resolved for both TX1 and TX2 cases. The results can be explained by revisiting expressions presented in 2.2.1. It is known that the width of the *sinc* function that represents the peak of the FFT is defined by the observation time as $\Delta f = 1/T_{obs}$. As T_{sweep} is not altered because it is a fixed parameter in the radar module, the width (in bins) of the FFT output *sinc* is the same for each bandwidth. However, the mapping from bins to distance is different, as the chirp slope depends on bandwidth. In fact, figure 4.10 shows how the range resolution improves (width of the *sinc* decreases) as bandwidth increases.

The reason why the profile on RX1 is chosen is that it is the closest antenna to the transmitter and therefore the effect of antenna coupling is observed. This is the explanation of the estimated positions for 50 and 100 MHz in figure 4.9. For such low bandwidths, the range resolution is large[5] and the radar can not separate the antenna coupling peak (the so-called *blind distance*) and the reflector peak. Thus, the peak value of the FFT for these two bandwidths appears at the wrong position, and in the case of TX2, the distance is resolved at 0 meters because it is the closest antenna to RX1. The profile peak due to antenna coupling masks the reflector peak so it can not be resolved.

[5]Large ΔR is not desired in terms of radar performance.

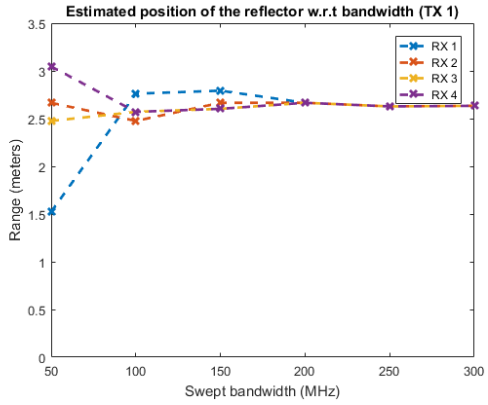

(a) 4 RX channels using TX1

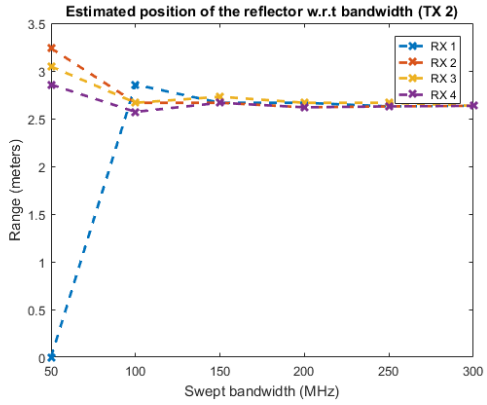

(b) 4 RX channels using TX2

Figure 4.9: Position of the reflector for different chirp bandwidths

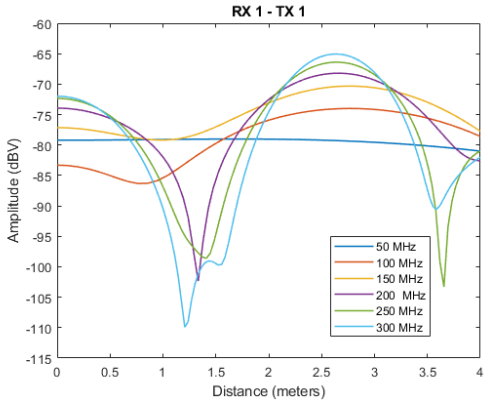

(a) RX 1 range profiles using TX 1

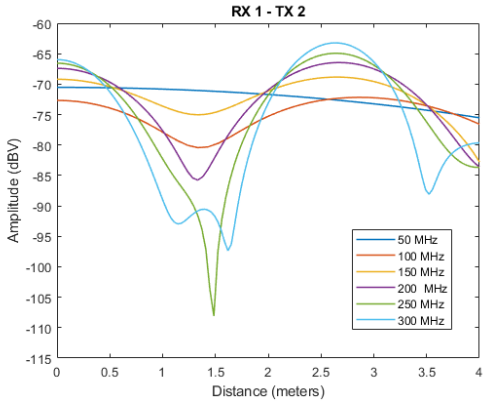

(b) RX 1 range profiles using TX 2

Figure 4.10: Range profile for different chirp bandwidths

4.3.2 Phase and velocity

The second step after the study of the radar range capabilities is to focus on the second observable that is presented in 2.2.2, velocity. The computation of velocity has been introduced in terms of applying the so-called 2-D FFT. It is computed both in range and along dimension two of the data matrix, or in other words, along the frame of chirps. The velocity is then extracted from the phase variations between chirps. It is important to note that computing velocities is only possible using chirp frames because the phase variation must be continuous. This means that the chirps under analysis must be transmitted continuously to preserve data completeness. In the current experimental set-up, velocity measurements have not been performed because of the complexity of setting up a proper system to generate moving targets inside the anechoic chamber. However, in this section the velocity computation routine is presented because it will also be used in the phase evaluation of the radar module.

Assume a 256×128 matrix that contains the 128 IF tones of a chirp frame received at RX1. The first step is the one explained in the previous section: computing the range FFT. The only difference is that the `fftshift` function is not applied because the shift will be performed over the whole matrix in two dimensions after the computation of the phase FFT. After applying the range FFT step, the matrix has size 4096×128 and each column is the range profile from each chirp. The next step is computing the FFT in dimension 2 using `NFFT_velocity` $= 2^8$. As it has been done when computing the range, a Hann window of length 128 is applied to each of the 4096 rows[6].

```
velocity_freqaxis = [-NFFT_velocity./2:NFFT_velocity./2-1].' ...
     ./NFFT_velocity.*(1/Cfg.Tp);
velocity = velocity_freqaxis*c0/(2.*fcarrier);
Win2DPhase_long = repmat(hanning(128).', numel(4096), 1);
PhaseScaWin = sum(Win2DPhase_long(1,:));
```

Note that in the range profile, the coordinate axis was computed transforming the FFT bins to frequency by means of the sampling frequency. In this case, there is also a sampling process: the chirp time. Each of the chirps takes a sample of the phase at an specific point in time. Therefore, to transform $NFFT\_velocity$ into frequency, the phase *"sampling frequency"* is to be considered as $1/T_p$, where T_p is 300 μs, the sum of up-ramp and down-ramp times. The velocity axis can then be computed by transforming the frequency axis using (2.3). In the end, the step of computing the 2-D FFT consists on two calls to the `ftt` function as in the following code box. After the whole matrix has been computed, the output is a 4096×256 matrix that can be plotted as a coloured image using range as the ordinate and velocity as the coordinate axis as in figure 4.11. This figure shows the typical *Range-Doppler* map: static targets are mapped at the centre (velocity equals zero) and in case there were targets with radial velocity, they would be mapped at either side. In the right when approaching the radar (positive velocity), and in the left side when departing (negative velocity). In this case, there is no moving target so the only resolved targets are the *blind distance* peak at 0 and the corner reflector at 2.571 metres.

```
range_profile = fft(data_rx1.*Win2D_long,NFFT,1).*FuSca/ScaWin;
range_doppler_map = fftshift(fft(range_profile.*Win2DPhase_long, ...
     NFFT_velocity, 2))./PhaseScaWin;
```

See that in the code above, the `fftshift` is performed in both dimensions. This reorders the matrix such that rows from 1 to 2048 correspond to the negative half of the range spectrum. At the same time, columns 0 to 128 correspond to velocities from $-v_{max}$ to 0 and 129 to 256 have velocities from 0 to v_{max}. In this case, v_{max} is 10.41 m/s.

[6]The window size is the length of the chirp frame, 128.

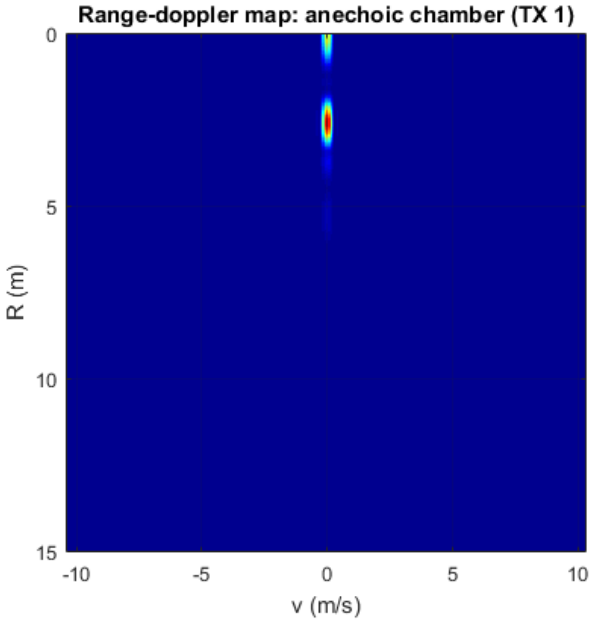

Figure 4.11: Range-Doppler map of the anechoic chamber set-up

Phase stability

In the range computation section a detailed study on the amplitude stability has been presented and in this section, a similar study is conducted on the phase. Knowing how does the platform respond under certain conditions is an important part of the design of a system. Error sources need to be detected and accounted for because they will affect the performance of the entire system. In this case, the phase is a key parameter in radar operation as the computation of velocity derives completely from it. So, as the initial step to check how stable the phase response is, the single-chirp measurement is considered.

The phase of the IF tone from which the range is derived, is directly computed from the range FFT. Note that, as presented in 2.2.2, the result of an FFT is a complex valued array. The absolute squared value of each bin yields the amplitude and the phase of the complex number yields the phase of the associated cosine. Therefore, it is important to look at the phase of the bin at which the reflector is resolved because it is the phase of the intermediate frequency (IF) tone that maps to distance. In figure 4.12 the phase at bin 82 of the four receiver channels, is plotted for an incident angle of 0 degrees.

See that the IF-tone phase that is computed by the radar is stable for single chirps. This is the expected result for an static environment like the one recreated inside the anechoic chamber, and the random variations that can be observed in a closer inspection are due to the noise-like contributions, for example the thermal noise on the RF front-end. Therefore, the variance of the phase in the single chirp measurement has been computed for channel 1 and transmitter 1 as $\sigma_w = 0.0278°$. This result has also been checked for the rest of RX-TX combinations

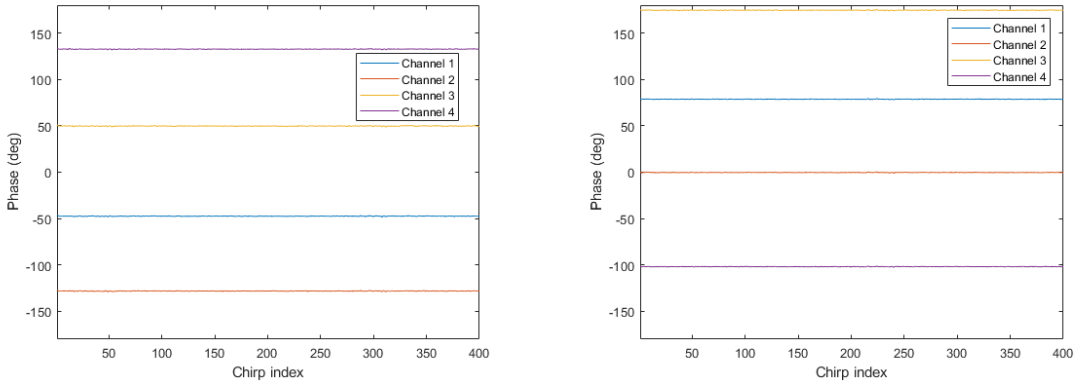

(a) Case TX 1 (b) Case TX 2

Figure 4.12: Phase of range-bin 82 along the 400 single chirps

and is assumed as the reference value for this random noise contributions. Note that it is very important to analyse the phase at a bin where the amplitude of the range profile is large because both the real and the imaginary part of the FFT output are large enough to mask the rounding noise added by Matlab. For bins at which the amplitude is low, the fact that Matlab does not output exact zero values rather than zero-like values (i.e. 10^{-15}), affects the result as $arctan\,(Im(x)/Re(x))$ will yield different angles for any small difference between the real and imaginary parts.

With the results shown above, the single-chirp phase stability is proven and now, the chirp frame is analysed. The same computations of the previous analysis are applied with the only constraint that the length of the frame is 128. Figure 4.13 shows the results achieved on each of the receiver channels for both transmitter antennas.

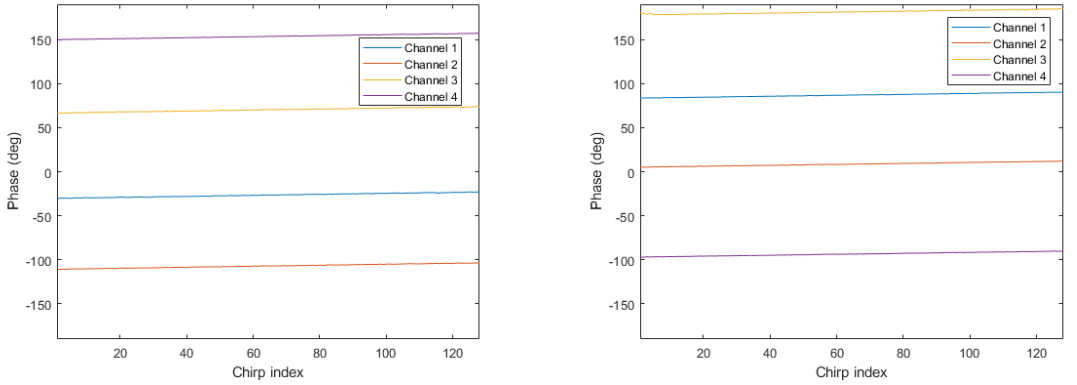

(a) Case TX 1 (b) Case TX 2

Figure 4.13: Phase of range-bin 82 along a frame of chirps

The presented figures show that the phase extracted from each chirp, at the bin at which

the reflector is resolved, is not constant as would be expected for a static set-up. See that the phase describes a positive ramp during the 128 chirps which means that there might be a moving object coming towards the radar. In the previous single-chirp study the variance was found to be σ_w, but for the frame of chirps there is a superposition of both the random behaviour and a systematic error that derives in a positive phase drift. Figure 4.14 shows a closer look at the phase at each channel for transmitter 1.

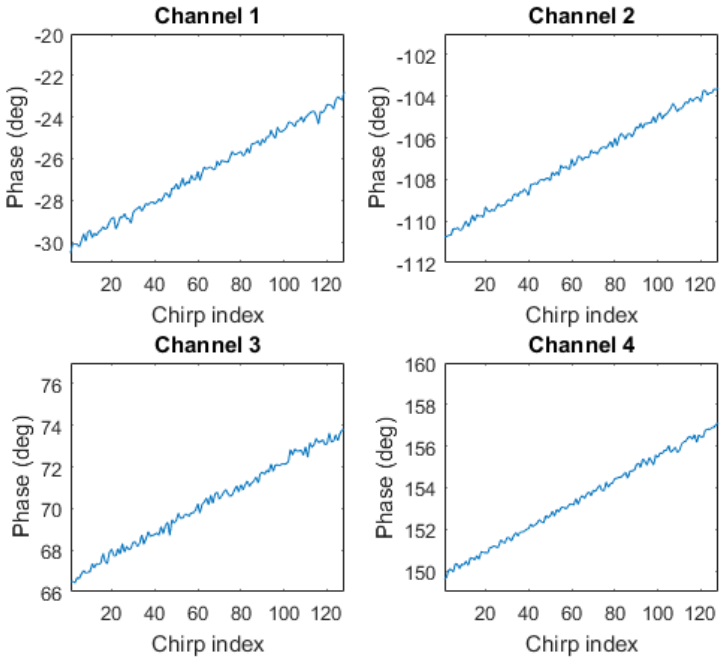

Figure 4.14: Phase of each RX channel for TX 1

In order to understand the unexpected result, the measurements were repeated and the entire set-up was checked to ensure that there were no moving parts that could be altering the measure. Once the repeated measures were processed and the same phase drift was observed, the situation was reported to the people at INRAS and they confirmed that this behaviour is far from optimal. The case is under study and they confirmed that the most probable reason for this phase instability is a clock drift between the reference clocks of the frequency synthesizer and the ADC module.

Figure 4.15 shows the result of subtracting the ramp to the phase response in order to compute the variance of the non-systematic error. The slope of the subtracted ramp is calculated from the average drift of the channels for a certain transmitter (see table 4.2). Then, the result of computing the variance of the phase without the systematic error yields $\sigma_{wframe} = 0.0294°$, a result that confirms that if the hardware instability is not considered, the phase variance is the same than in the single chirp case.

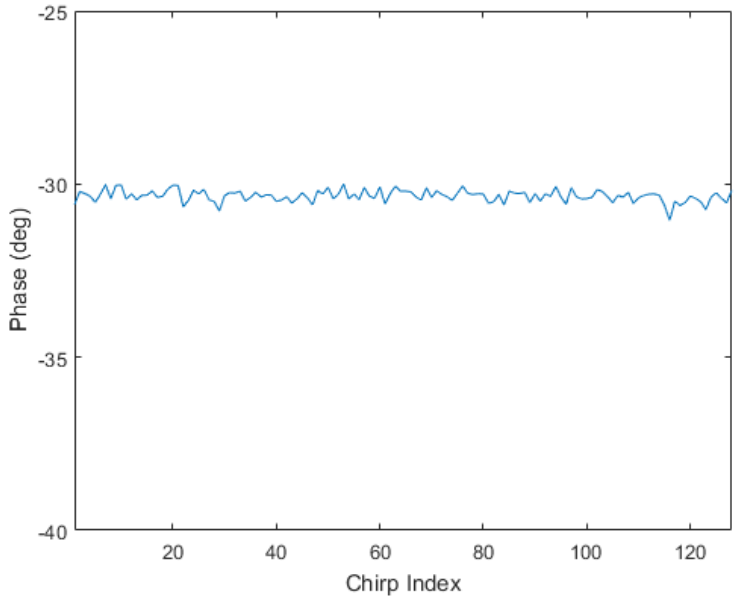

Figure 4.15: Phase response over a frame without system drift

Channel	Drift (°)	v_{offset} (m/s)
RX 1	7.3	0.0066
RX 2	7.76	0.007
RX 3	7.5	0.0068
RX 4	7.1	0.0064

(a) Case TX 1

Channel	Drift (°)	v_{offset} (m/s)
RX 1	6.5	0.0059
RX 2	6.55	0.0059
RX 3	4.9	0.0044
RX 4	6.69	0.006

(b) Case TX 2

Table 4.2: Phase drift and velocity error on a 128 chirp frame

In terms of estimating how does the phase noise affect velocity, the propagation of the error from phase to velocity needs to be studied. See that the phase behaviour can be defined as, $\phi(t) = \phi_0 + \sigma_n + \sigma_s t$, where σ_s is the slope of the drift, caused by the systematic error. Recalling (2.3) and that the frequency is the derivative of the phase over time, a ramp in phase will be translated to a velocity offset. Additionally, the random noise contribution will still be overlaid to the velocity. Table 4.2 shows the total phase drifts for every receiver-transmitter combination and the offset that this drift causes to the velocity estimation. As it can be seen, the velocity offset is well below the velocity resolution (see 3.3) and therefore, the effect of this phase drift, although not desired, is negligible. However, note that if the frame length could be increased, the velocity resolution would improve and at the point where the drift would sweep 90° during a frame, the systematic error would not be negligible.

4.3.3 Direction of arrival

The two-dimensional Fourier transform has been introduced in the previous section as the means to compute velocity along with the range in a frame of chirps. This confirmed the reasoning behind structuring the data in $256 \times NumChirps$ matrices, as one per channel. However, recall that the output from the radar module processor is a $256 \cdot NumChirps \times 4$ matrix, where each column is a receiver channel. In this section the 2D-FFT procedure is the basis for angle of arrival estimation but the difference lies now in the fact that the data to be processed, is kept in the format at which it is output from the radar.

As introduced in section 2.2.3, the information concerning the direction of arrival is contained in the phase difference between channels for a fixed instant in time. This difference has already been observed in figure 4.13 where the plotted data corresponds to a 0° arrival scenario. Therefore, that case can be understood as the reference phase between receiver channels that is caused by the geometrical distribution of antennas on the radar board and the different propagation distances from the transmitter to each of the receiver antennas. In terms of angular estimation the definition of a reference transmitter is key and in this case, transmitter 1 is selected. The phase variations will then be computed based both on the reference and a set of calibration coefficients that take into account the spacing distances presented in table 3.1.

Calibration coefficients

The phase reference at an angle of arrival of 0° mentioned above is a figure of importance in any radar framework, because it defines the calibration coefficients that are needed to map phase variations unambiguously. Recall that the phase of a signal is not an absolute value rather than a relative one. Thus, a reference frame is always needed to extract information from phase variations.

The calibration coefficients are measured based on data from a specific set-up where the reference corner reflector is completely aligned with the phase centre of the reference transmitter. By ensuring this, the geometric problem is uniquely defined and results are complete. The DemoRad platform has an internal EEPROM memory that contains the set of calibration parameters measured at INRAS, and some additional information about the calibration set-up [INR17]. The calibration coefficient is a complex number whose norm accounts for the amplitude of the channel, and whose phase corrects deviations between channels. Therefore when calibration coefficients are applied to data, each of the data values is being multiplied by a complex exponential that equalizes amplitude on all channels (with respect to a reference RX-TX pair), and ensures that phase shifts between channels are equal. Note that due to hardware imperfections on the patch antennas, although being spaced at $\lambda/2$ the phase differences between them are not exactly the same (figure 4.12). Coefficients are the corrections that are needed so that

Tx - Rx pair	Norm	Real part	Imaginary part	Phase (°)
RX 1 - TX 1	1.0892989	-1.0743707	0.17972141	170.5035
RX 2 - TX 1	1.0829163	0.045028188	-1.0819798	-87.6169
RX 3 - TX 1	1.1036194	0.19568112	1.0861329	79.7870
RX 4 - TX 1	1	1	0	0
RX 1 - TX 2	0.8910009	0.17526488	0.87359306	78.6556
RX 2 - TX 2	0.90371766	-0.88566121	0.17974931	168.5274
RX 3 - TX 2	0.96110547	0.9520472	-0.13164297	-7.8726
RX 4 - TX 2	0.78819556	0.031341046	-0.7875722	-87.7211

Table 4.3: Calibration coefficients and angle

the transmitter and the four receiver antennas are placed along the same exact baseline. Table 4.3 shows the calibration coefficients that are stored in the DemoRad memory and the phase of each one. According to the INRAS report, the measurements were performed using a 0 dBm^2 corner reflector, at a distance of 5 metres.

See that the reference pair is RX4 - TX1, the ones that are furthest from each other, and that there are eight calibration coefficients even though only four physical receiver antennas exist. The reason behind this is enabling MIMO operation with a 7 element virtual antenna array. If the entire set of coefficients are applied in the way that is explained in the following *MIMO DoA* section, a virtual array like the one shown in figure 4.16 is achieved, thus yielding higher angular resolution.

4.3.3.1 Standard DoA

Let `Data` be a 256×4 matrix that contains the samples of one chirp. Previous to any FFT computation, the first step is to access the calibration data from the board using the specific function `CalDat = Brd.BrdGetCalDat();`. However, if the data to be processed is already stored in files, the coefficients can be loaded from a previously saved *.mat* file. In the following code box, some specific parameters that are needed to compute the angle of arrival are presented.

The calibration matrix is a 256×4 matrix where each column is a repetition of the calibration coefficient of the respective channel. See also that another time a Hann window is used in the angular FFT. As there are only four spatial samples, it is a small window and therefore resolution is limited.

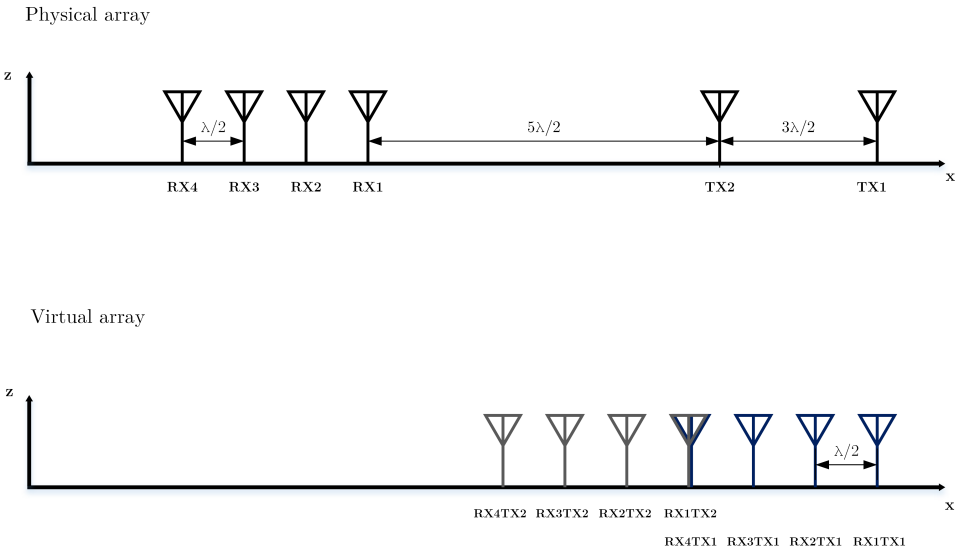

Figure 4.16: Virtual 7 element array

```
CalDat      = Brd.BrdGetCalDat();
CalDatTx1 = CalDat(1:4);
CalDatTx2 = CalDat(5:8);
calibration_matrix1     =   repmat(CalDatTxi.',N ,1);

NFFTAngle          =   256;
WinAngle           =   hanning(4);
ScaWinAngle        =   sum(WinAngle);
WinAngle2D         =   repmat(WinAngle.',numel(range_axis),1);
```

Additionally, the mapping of the FFT output to angle must also be defined, while the range mapping function has already been used both in range and velocity evaluation sections. In the code box below, the angle axis is created and the angular 2-D FFT is presented.

```
angle_axis  =   asin(2*[-NFFTAngle./2:NFFTAngle./2-1].'./NFFTAngle)./pi*180;

Range   = fft(Data(1:256,:).*calibration_matrix1.*Win2D, NFFT, 1).*FuSca/ScaWin;
DoA_FFT = fftshift(fft(Range.*WinAngle2D, NFFTAngle, 2)/ScaWinAngle);
```

Following the same philosophy that was applied to jointly compute range and velocity, the angle-range map is obtained. See that the main difference is that the calibration matrix is multiplied with `Data` and the range Hann window, before applying the range FFT. After that, the angle FFT is applied in dimension two, and the spectrum is shifted on both matrix dimensions. The end result stored inside the `DoA_FFT` matrix is 4096×256 where the first 2048 correspond to the negative half of the range spectrum, that does not have a physical meaning, columns 1

to 127 contain negative angles and columns 128 to 256 map the positive ones. The angle axis is computed from the definition in figure 2.7 because the FFT in dimension two transforms to the wave number domain ($k = 2\pi/\lambda$) and the spacing d is $\lambda/2$. A wide range of plots can be shown once this range-angle matrix is computed, for example a range versus angle map or a polar plot in x and y coordinates. As a first step, the most straightforward representation is the range-angle map. Figure 4.17 shows two different plots of the same map. Note that because of the limited number of space samples a certain amount of noise is generated where there are no targets. If these results are directly plotted in a colour map, the result can become confusing as in 4.17a. Therefore, the actual strategy is to normalize the result to the largest peak and set a threshold below which all values will be mapped to zero. In this case, the threshold is set to -18 dB and the result is shown in figure 4.17b.

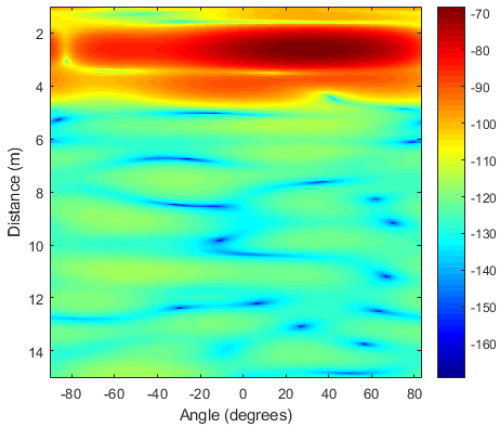

(a) Direct map

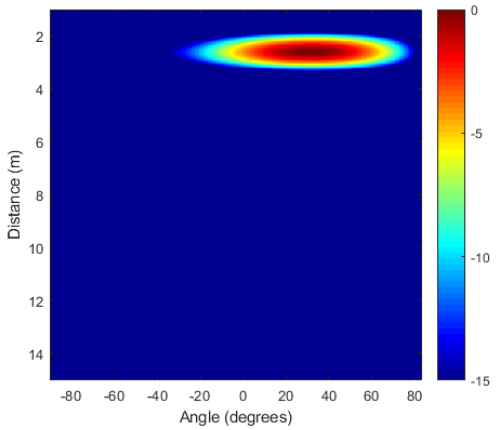

(b) Normalized map

Figure 4.17: Range versus angle map of the anechoic chamber (DoA = 24°)

4.3.3.2 MIMO DoA

At the beginning of chapter 3 the MIMO mode was presented briefly as a sort of combined operation between transmitter antennas 1 and 2. In fact, when the MIMO flag is set to 1 and a frame measurement is taken, the output is another time a 256×128 matrix per channel but with the difference that odd columns of this matrix contain chirps emitted by transmitter 1 and even columns, the ones from transmitter 2. As in the previous section, the desired data format for DoA computation is a $256 \times NumChannels$ matrix and therefore it has to be reshaped. Assume that `Data1`, `Data2`, `Data3` and `Data4` are the matrices of each channel. To compute DoA using MIMO data, two columns from each of the matrices will be used to compose the so-called `DataVirt` matrix. This matrix will have dimensions 256×7 where columns 1, 2 and 3 will be `Data1(:,1), Data2(:,1)` and `Data3(:,1)`, each one multiplied with the first three calibration coefficients (transmitter 1), and columns 5, 6 and 7 will be `Data2(:,2), Data3(:,2)` and `Data4(:,2)` each again multiplied with calibration coefficients 6, 7 and 8 (transmitter 2). The central element of the virtual array is the overlapped one, and it is a combination of reference element RX4 - TX1 and RX1 - TX2. Therefore, column four of `DataVirt` will be `0.5*Data4(:,1)*calibration_coeff(4) + Data1(:,2)*calibration_coeff(5)`. Once the matrix is shaped, the same steps defined in the previous section can be computed with the only difference that now the angular Hann window will have 7 elements. See that as calibration has been applied when conforming the matrix, there is no need to add that multiplication in the `fft` call.

Equation 2.14 stated that the angular resolution of the radar for a $\lambda/2$ antenna spacing depended on the number of elements of the array, for the same incident angle. Therefore, using the virtual antenna arrangement the resolution has increased. Figure 4.18 shows a comparison between the two cases: standard and MIMO DoA computation. In table 3.3 the angular resolution is calculated for a 4-antenna array as $\theta_{res1} = 28.64°$. Applying the same equation, for a 7-element array, the resolution is now $\theta_{res2} = 16.37°$ as shown in the figures. See that equation 2.14 defines the resolution in one angular quadrant. As positive and negative angles are now plotted, the resolution θ_{res} is the angle from the peak to a -3 dB fall and the total width of the *sinc* in angle is $2\theta_{res}$.

Additionally, one interesting characteristic of this type of maps where two radar observables are jointly computed, is the different resolutions in each dimension. It can be seen that the range resolution is 0.5 metres for both the MIMO and the standard case, what is a rather obvious result because the resolution only depends on the amount of samples used in the FFT step.

In terms of angular resolution, figure 4.19 shows the spatial spectrum at the range bin where the reflector is resolved. It is clearly shown that the *sinc* width is larger for the standard DoA case. As the final example of the DoA section of this project, figure 4.20 shows the polar

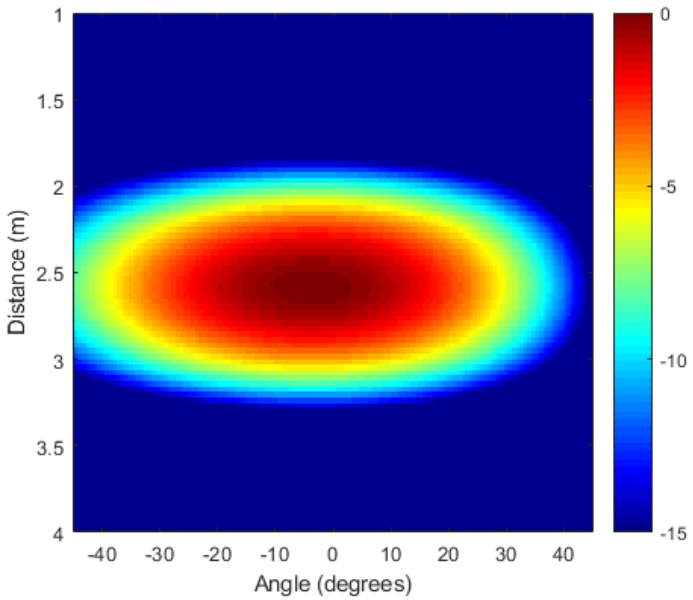

(a) Standard DoA

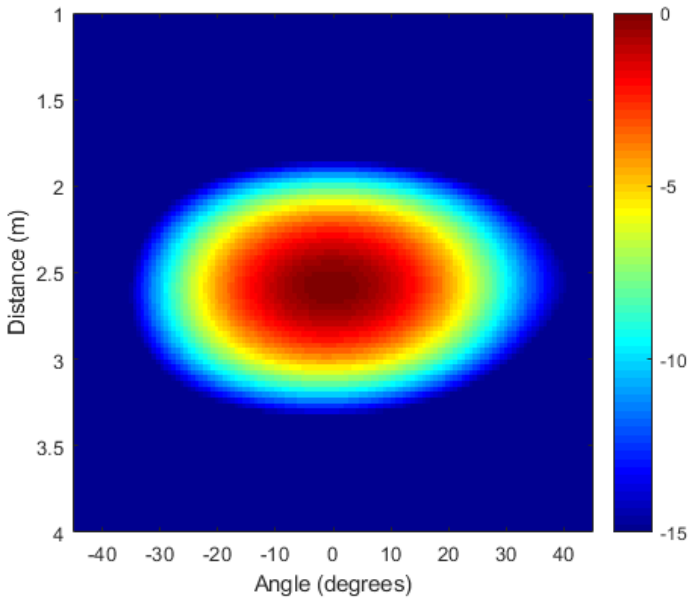

(b) MIMO DoA

Figure 4.18: Range versus angle map resolution (DoA = 0 °)

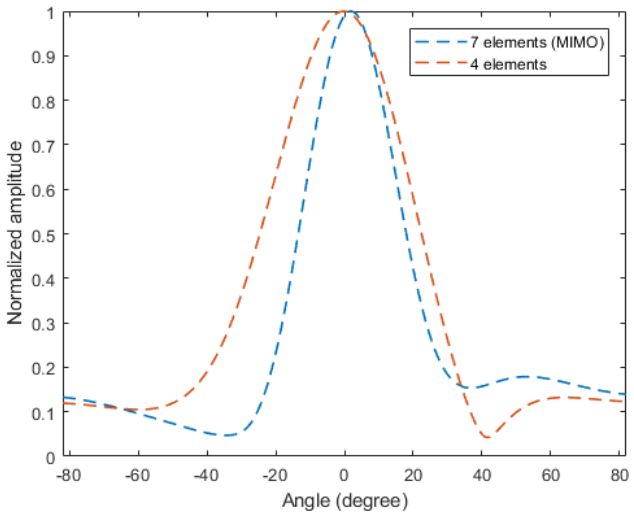

Figure 4.19: Comparison of spatial spectra at resolved position of the reflector

representation of the chamber scenario for an incident angle of -45 degrees.

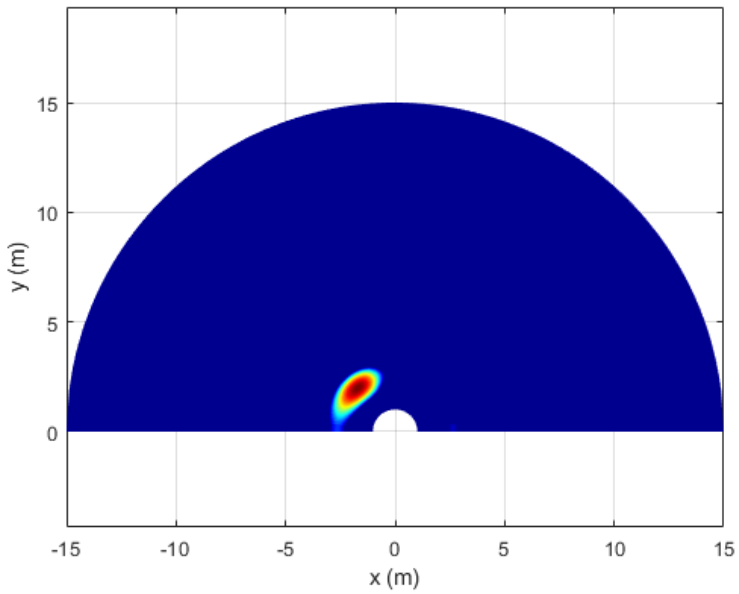

Figure 4.20: XY plot of the chamber scenario (DoA = -45 °)

4.3.4 Additional measures

Apart from studying the three main radar observables, other conclusions can be extracted from the analysis of the measured data from the different scenarios recreated inside the chamber. One of these alternative measurements is the variation of the amplitude yielded by the reflector

for different angular positions. The first result corresponds to an scenario like the one used to simulate DoA: radar is moved while reflector is kept fix. The variation of the received power with respect to the incident angle is shown in figure 4.21 for both transmitters. See that what is obtained is an approximation of the antenna radiation pattern due to the reciprocity principle [Car02]. The shape of the results matches the pattern shown in figure 3.3.

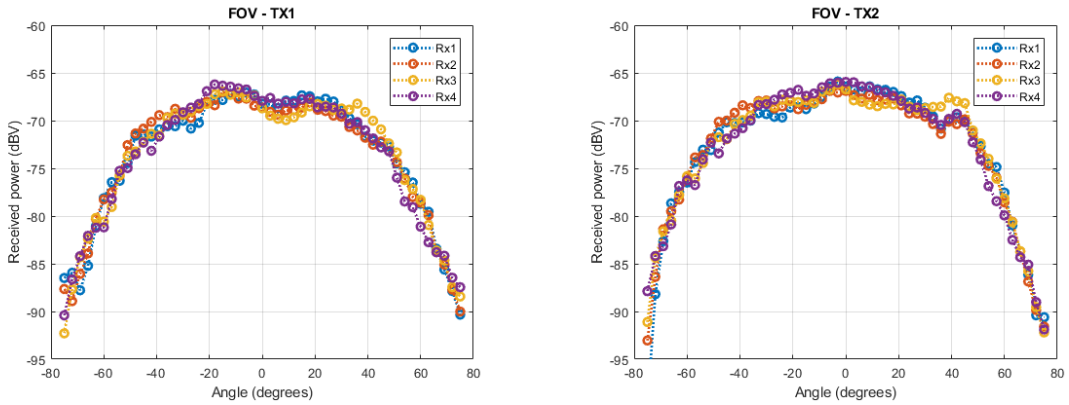

(a) Case TX 1 (b) Case TX 2

Figure 4.21: Field of view of the radar platform

Furthermore, in order to characterise the trihedral reflector, the set-up was changed and the radar was mounted on the probe pole of the chamber. Another time the same measurement was taken changing the angular position of the reflector (on the DUT), and results are shown in figure 4.22. The achieved pattern matches the theoretic result obtained through simulation with FEKO.

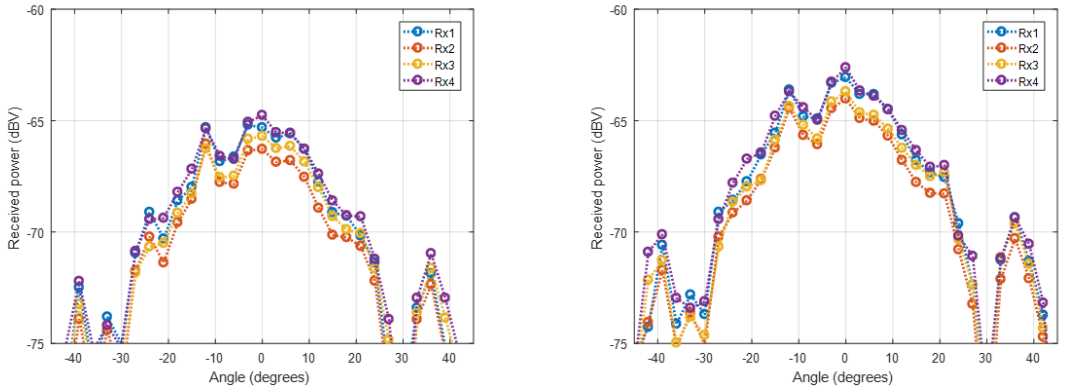

(a) Case TX 1 (b) Case TX 2

Figure 4.22: Field of view of the trihedral reflector

4.4 Why phase matters

The role of the phase to estimate a target's velocity is key and is the motivation behind the stability analysis. However, other possible applications can be conceived from the observation of the phase behaviour with respect to time. In the beginning of this project, the range resolution of the radar was found to be 0.5 meters. Nevertheless, see that through phase observation, displacements in the order of $\pm\lambda/4$ can be tracked. This describes a whole new range of applications where small movements have to be detected. For example, one of them might be the control of vibrations in industrial machinery or the tracking of a patient breath pattern. In fact, if a movement is repetitive in the order of the radar chirp time and small enough to fall in the $\pm\lambda/4$ region, it can be easily detected by analysing the variation of the IF tones. Figure 3.5 showed the time-domain representation of the IF tone from a chirp. In case there was a periodic movement to be tracked, the pattern would swing from left to right because the phase would be changing.

Additionally, there are also other applications of the phase observation in the automotive sector. Mounting the radar on a vehicle is the main objective behind platforms like the one under analysis in this project, but it is not an straightforward step as it has to be hidden behind some other car parts, either the bumpers or other radome structures. In the case of a well-known car brand, the front radar is hidden behind the car insignia. Although they are made of a dielectric material, the insignia itself creates a perturbation of the wave propagation and therefore it needs to be thoroughly calibrated. Assume now that the insignia is hit by an object and is slightly tilted towards one side. The radar calibration will not be perfect any more and will have to be corrected. However, the modifications created by this slight tilt will be observed in the phase of the IF tones, because the propagation paths will have changed compared with the calibrated ones. The need of low-cost re-calibration solutions is a strong topic for automotive companies and thus an interesting field for further research. Radar sensors have an extensive amount of applications in a wide range of sectors, and the migration from the 24 GHz ISM to the 77 GHz dedicated band, is driving the market to even more fascinating developments.

Chapter 5

Target emulator

Due to the high safety implications of the automotive sector, any novel solution is subject to an extensive amount of certification tests and examinations by the regulatory offices. At the same time, designers struggle with the difficulty of testing such solutions. See the case of a self-driven car equipped with radar sensors that need to be tested. Until now the straightforward approach was to use the car on a dynamo and software-simulate targets in front of it. Nevertheless, there is no actual radar hardware operation in this tests.

Nowadays, modern testing is driven by the *hardware-in-the-loop* philosophy, where simulations are performed by actually deceiving the hardware. However, although surely fun, it is not usually feasible to let an autonomous car in an isolated circuit to throw objects in its way. The market demands a solution that can emulate targets at different range positions and velocities, while the car is in the lab. Such a solution is presented in this chapter.

5.1 Hardware in the loop

Now that connected vehicles are top trend and with the increasing amount of automated functionalities that are released in the automotive sector, the until now valid approach of software simulations has been outdated. More car manufacturers every time are trying to incorporate the hardware-in-the-loop principle in their testing set-ups. This type of testing is based on deceiving the hardware sensor itself rather than the system as a whole. For example, testing the antilock brake system (ABS) of a vehicle by making it brake suddenly on a dynamo instead of simulating the electric signals that the central computer would receive in case there was a sudden brake. In the case of automotive radar this problem becomes even more complicated because front-view radars are designed to control up to 200 metres ahead of the vehicle. The perspective of setting up a 200 metre long test room just to assess the performance of a system does not seem realistic.

Then how can a radar manufacturer test that a car is capable of detecting a pedestrian that suddenly crosses the street in front of the vehicle? This has been a topic of deep study in the past few years and some companies have started providing their own devices. The topic is now centred in developing low-cost technologies that can be used to test and calibrate radar systems. Note that such a solution involves some sort of device that can deceive the radar with signals that map to targets, but in order to do so, a deep knowledge of how range and velocity are generated in FMCW radar systems is needed.

5.1.1 Range emulation

From the theoretical introduction presented in chapter 2 it has been shown that peaks in the range profile are obtained because of the time delay that is introduced between the emitted and the reference chirps. In the anechoic chamber the reflector is always at a position of 2.55 metres and then the propagation delay is always the same, but if another delay is added to the emitted signal, the IF tone will have a higher frequency and therefore will be mapped to a larger distance from the radar. Thus, emulating a target in range can be understood as adding a certain delay to the emitted signal. The addition of such delay can be achieved with, for example, a transmission line of a certain length. If the emitted signal is received by an antenna, fed to a transmission line and then re-radiated back to the radar, the signal that is received at the radar, will be delayed a time $\tau_d = l_{line}/c_0$ where l_{line} is the length of the transmission line and c_0 is the speed of light in vacuum. This idea might seem interesting but see that the real length of the line is proportional to the real propagation path that the chirps would have travelled. Therefore, such delay addition would have to cope with losses due to the line, physical limitations in size and with the fact that the modification of the delay would be hard if not impossible. Solutions to this problem have been presented by transforming the RF to an optical signal and applying variable delay optical fibre lines [Lut14, Eng16]. However these solutions are complex and high-cost, what falls out of the low-cost scope of automotive radar solutions.

Nevertheless, another option to achieve range simulation should be considered. Notice that the chirp IF tone derived from the time delay between reference and received chirps. Thus, the larger the delay, the higher IF and therefore, a way of achieving a certain IF tone after mixing could be adding a frequency shift on the chirp signal itself as in figure 5.1. If the signal is received, then mixed with the desired frequency tone and re-radiated back to the radar, the desired IF tone would be generated at the mixer of the radar. A similar solution has been found in the literature with low-cost radar calibration purpose [Sch17] but rather limited in terms of frequency.

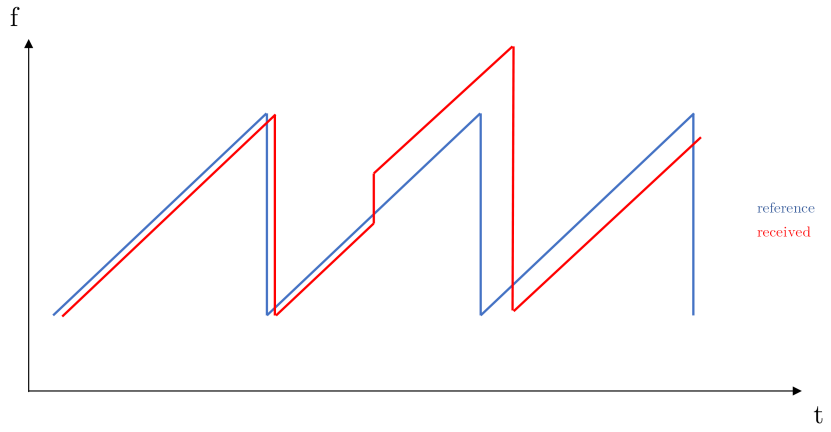

Figure 5.1: Chirp with frequency shift

5.1.2 Velocity emulation

Velocity in FMCW radar sensors is computed from the phase variation of the IF tone along a frame of chirps, as it has been stated in 2.2.2. In a real environment, the phase suffers a continuous variation because of the physical displacement of the target. Then, emulation of a target will involve adding such a phase variation to the signal before re-radiating it. This addition, that can be understood as a phase modulation, can be performed by using a vector modulator. These devices are capable of altering the phase of the output signal, based on the voltage differences of two DC signals, that are normally digitally generated.

5.1.3 RCS emulation

Apart from emulating position and velocity, the radar cross section of the target under simulation must be considered as the automotive environment is wide in terms of the detectable targets. See that the RCS of targets such as kids and human-beings completely differs with the one of trucks or other big obstacles. Therefore, the ability to simulate a target whose RCS can be modified is interesting. The radar range equation in (2.2) defines that the cross section of a target is related to the received power and thus, the implementation of an amplification stage at the radar emulator would yield the possibility to alter received power. Note that adding an amplifier is not completely straightforward and requires a careful study of the non-linearities of the device. Intermodulation products are potentially detectable as range IF tones if not correctly handled.

5.2 Proposed solution

From the previous approach to how radar observables can be generated, it can be seen that the overall structure of the system will consist of two antenna elements, one to capture the emitted chirps and the other to re-radiate the signal, and a modulation stage connected in-between the two. An schematic of the proposed stage is shown in figure 5.2. See that in this test scheme, the frequency shifting and the phase modulation stages have been separated to simplify the explanation even though they can be jointly implemented.

As an initial implementation of a prototype, range is the selected observable to be emulated. Whereas, an explanation of how velocity will be implemented in the future is also given. The following list depicts the elements that have been selected for the implementation of the prototype:

- HMC1063LP3E 24 GHz IQ mixer from Analog Devices.
- SWC-42KM-R1 K-Band Waveguide transition.
- Low-frequency 90° hybrid.

5.2.1 Single-sideband mixer

The initial idea that might come to ones mind if a signal is to be frequency shifted, is using a mixer. The mixer is a well-known 3-port device that allows up- and down-conversion using a local oscillator signal, and that is present in most RF front-ends. However, if the radar platform parameters are considered, some limitations arise. See that the emitted signal is a 300 MHz-wide chirp at a frequency of 24 GHz and a ramp-up time of 260 μs. With these and (2.5) it can be seen that to generate a target within the unambiguous range of the radar, the IF frequency must be between 0 and 500 kHz. Therefore, the situation of the mixer that would implement the shift would be a LO signal of 250 kHz (for a target at around 30 metres) mixing a 300 MHz-wide chirp. The up- and down-converted results of the mixing stage would be almost completely overlapping as the total bandwidth is way larger than the frequency shift. The result then, would not be a chirp any more.

After a thorough study of the problem, the solution was found to be a single-sideband mixer [Kea17]. This device is composed of a power splitter, two mixers and two 90° hybrids distributed as shown in figure 5.3b. See that the incoming signal is split in two different paths, each one connected to a mixer whose LO port is fed in quadrature from the same LO frequency source. After the mixing stage, both channels are fed into the second quadrature hybrid and

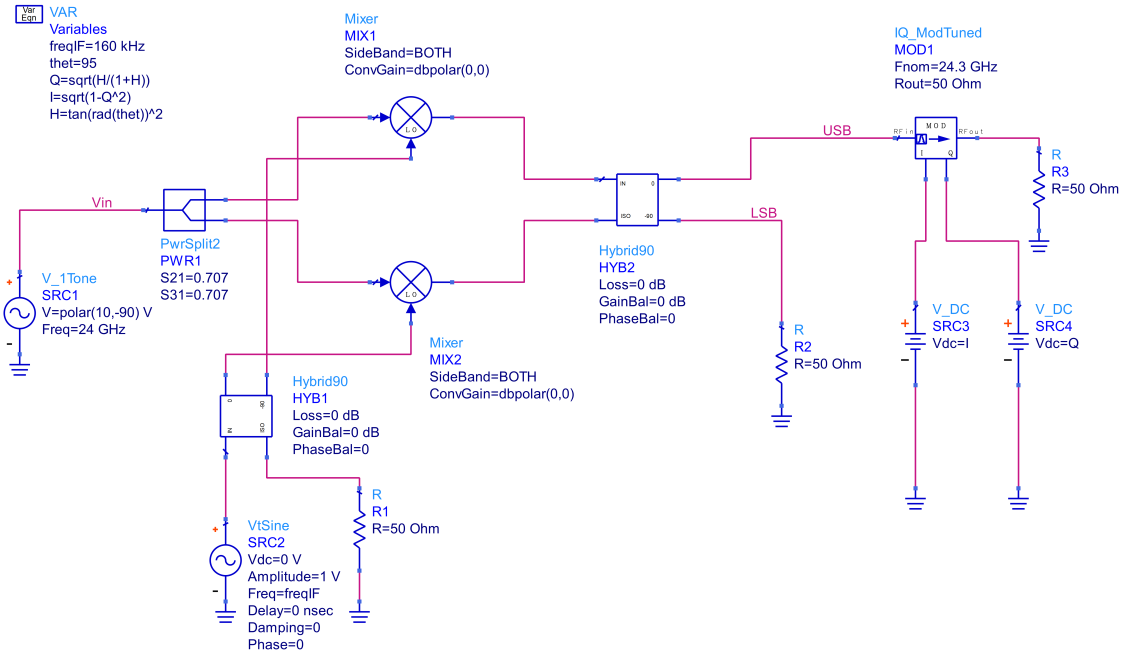

Figure 5.2: Target emulator schematic

the two outputs are either the lower-side band or the upper-side band depending on which port is selected.

The SSB mixer used in this project has been selected because the IF ports can handle a frequency range from DC to 3 GHz and the LO and RF ports can handle frequencies from 21 to 30 and 24 to 27 GHz respectively. Figure 5.3a shows the internal elements integrated in the Analog Devices IQ Mixer. See that there are two different IF ports that must be fed in quadrature if single-sideband up-conversion is desired. At the same time, the fact that the IF ports can handle DC voltages opens the possibility of jointly emulating range and velocity if the IF signals are also altered in amplitude. See that if the two IF are not of the same amplitude, the superposition of the signal coming from the two quadrature paths (i.e. each of the mixers) at the RF output port, will yield a signal whose phase is the angle between the in-phase and the quadrature amplitudes.

$$\phi = \arctan\left(Q/I\right) \tag{5.1}$$

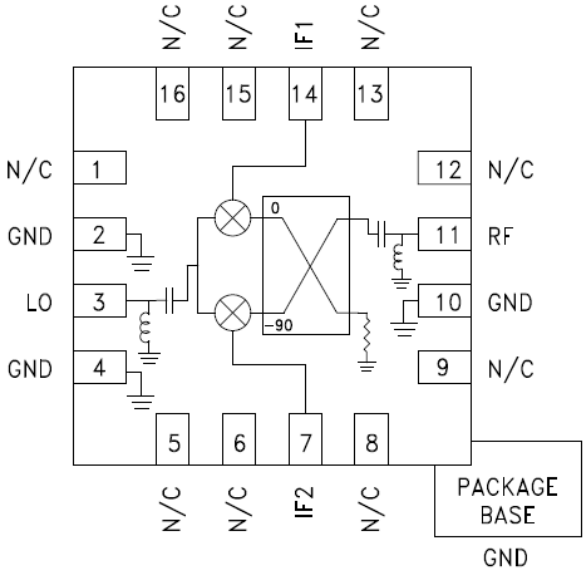

(a) Layout of the HMC1063LP3E IQ Mixer

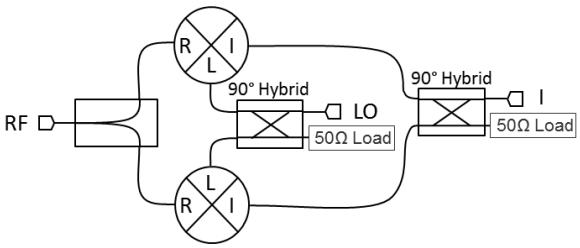

(b) Single-sideband mixer schematic (Source: Marki Microwave)

Figure 5.3: Single-sideband mixer model

5.2.2 Low-frequency quadrature hybrid

In the previous section the order of magnitude of the IF tones has been stated at the LF (low-frequency) band and such low frequencies make finding a commercial quadrature hybrid almost impossible. Wavelength is in the order of hundreds of metres and such dimensions make the implementation of typical micro-strip branch-line topologies infeasible. In order to tackle this limitation, the design of a hybrid is accomplished but because of the limited bandwidth of hybrid couplers, some of the emulation characteristics need to be bounded.

Considering that the measurement environment is an anechoic chamber and that the corner reflector is mounted at a distance of 2.55 metres of the radar, the emulation of a target within the 15 to 30 metres range would be interesting in terms of clearly comparing both targets. With these and using (2.5) the desired intermediate frequency lapse is found from 115 to 190 kHz.

5.2.2.1 Lumped element hybrid coupler

The first implementation of the hybrid is designed based on the lumped element equivalent of a transmission line. This model consists on an LC (inductor and capacitor) parallel structure, and the symmetrical replication of this LC cell in a formation such as the one shown in figure 5.4 will yield the hybrid coupler behaviour [Bre09]. The calculation of the L and C values is achieved via the well-known equations that follow, where Z_0 is the characteristic impedance of the line, and f_{3dB} is the LC cell resonance frequency.

$$Z_0 = \sqrt{\frac{L}{C}} \tag{5.2}$$

$$L = \frac{Z_0}{2\pi f_{3dB}} \tag{5.3}$$

$$C = \frac{1}{2\pi f_{3dB} Z_0} \tag{5.4}$$

Additionally, in consideration of impedance matching to 50 Ω, see that cells between ports 1-4 and 2-3 have an impedance of Z_0 while cells connecting 1-2 and 3-4 are $\sqrt{2}Z_0$ matched. Finally, 160 kHz is chosen as the design frequency and the capacitance and inductance values shown in figure 5.4 are calculated.

An S-Parameter simulation of the design has been carried out using ADS in order to see the bandwidth at which the device is balanced both in amplitude and phase. Figures 5.5a and 5.5b show the amplitude and the phase imbalance of this design, respectively. See that the bandwidth at which the device is balanced both in phase and amplitude is narrow. Therefore, the SSB will only be able to refuse the lower-sideband from approximately 150 to 170 kHz, what will result in emulable targets only in the range from 19 to 21 metres.

This model has been implemented so that the concept of the radar emulator could be tested while the components needed for the design proposed in the next section were delivered. This lumped hybrid prototype has been implemented using an FR4 substrate plate where the landing pattern of the lumped elements has been milled. The lines connecting the elements and the ports are 2 millimetres wide and due to the low operation frequency, the electrical length of these lines is negligible. In figure 5.8 the physical implementation of the lumped hybrid coupler is shown on the left side.

5.2.2.2 Broad-band transformer-based hybrid coupler

The need of a broad-band coupler that allows a wider emulation in range can be fulfilled by changing to another topology that is based on the use of highly coupled inductors [Ho89].

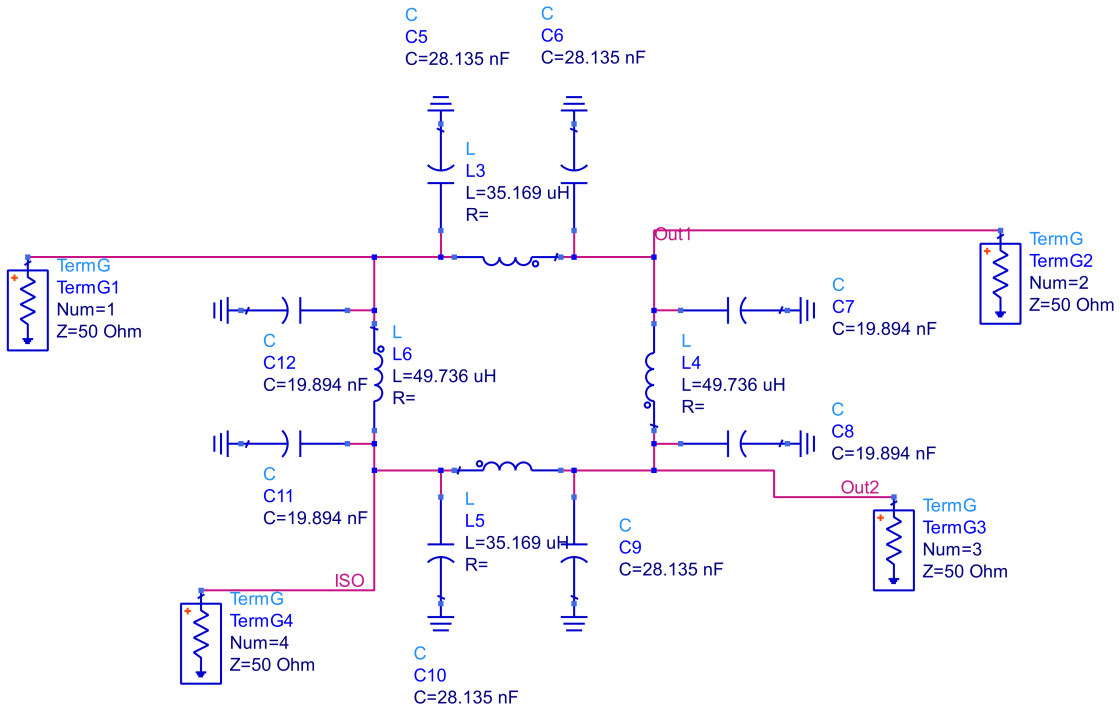

Figure 5.4: Schematic of the lumped element hybrid coupler

This inductors are achieved by the means of a bifilar coil wound around a ferrite toroidal, thus conforming a transformer. Then, the basic structure consists on a parallel topology of two capacitors and the coupled inductor. The aforementioned equations still apply for the calculation of the inductor and capacitor values of the transformer cell, being L and C/2 the values of the inductor and the capacitors respectively.

If a single transformer in parallel to two capacitors is evaluated, the topology yields a broadband quadrature phase response, but amplitude balance only occurs at the design frequency. Achieving broadband response in both phase and amplitude is possible through concatenation of transformer cells via a 24° delay transmission line [Fis73]. As in the lumped case, the implementation of such delay will be accomplished via an LC model of the line. See that using $\beta = \omega\sqrt{LC}$, and (5.1), results shown in figure 5.7 are obtained.

The results of the ADS simulation are depicted in figures 5.6a and 5.6b and it can be seen that the a broader balanced band has been achieved both in amplitude and phase, specially noting that the phase balance is quasi-optimal.

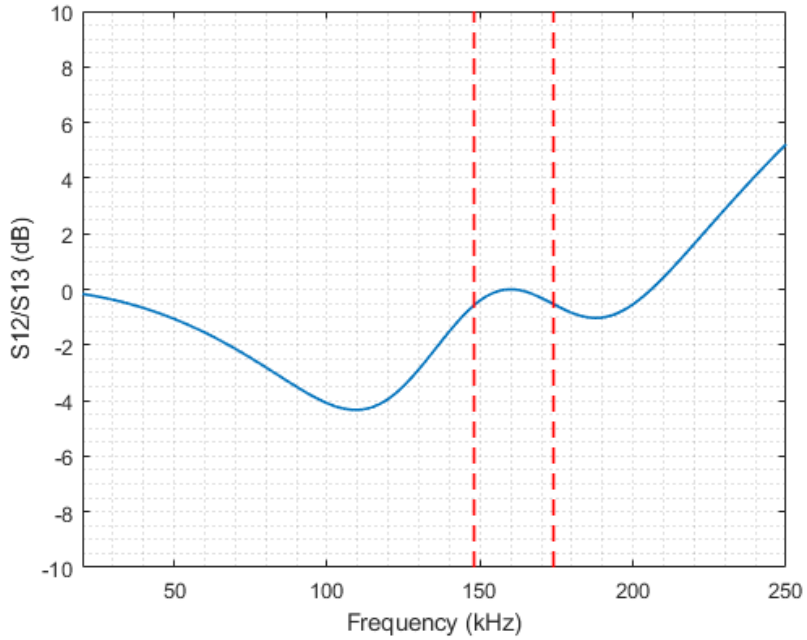

(a) Amplitude Imbalance

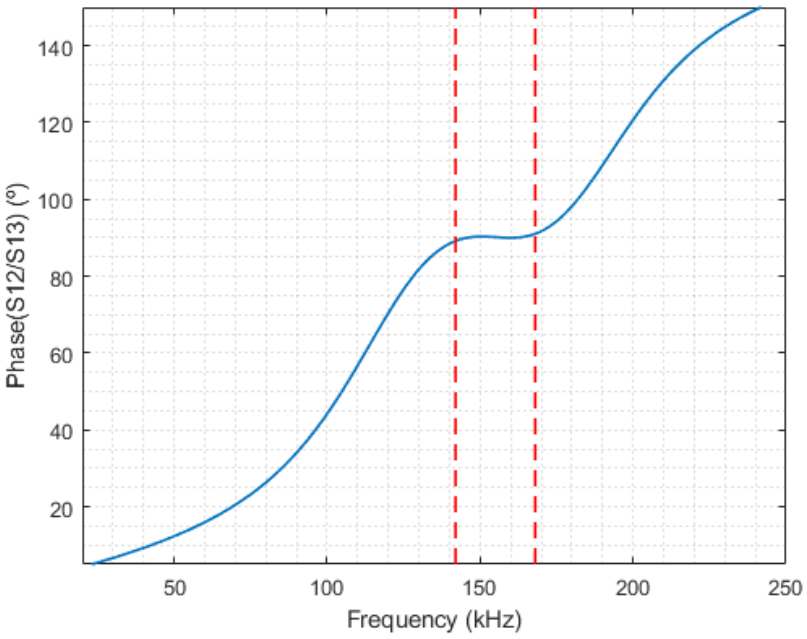

(b) Phase Imbalance

Figure 5.5: Simulation results of the lumped element hybrid

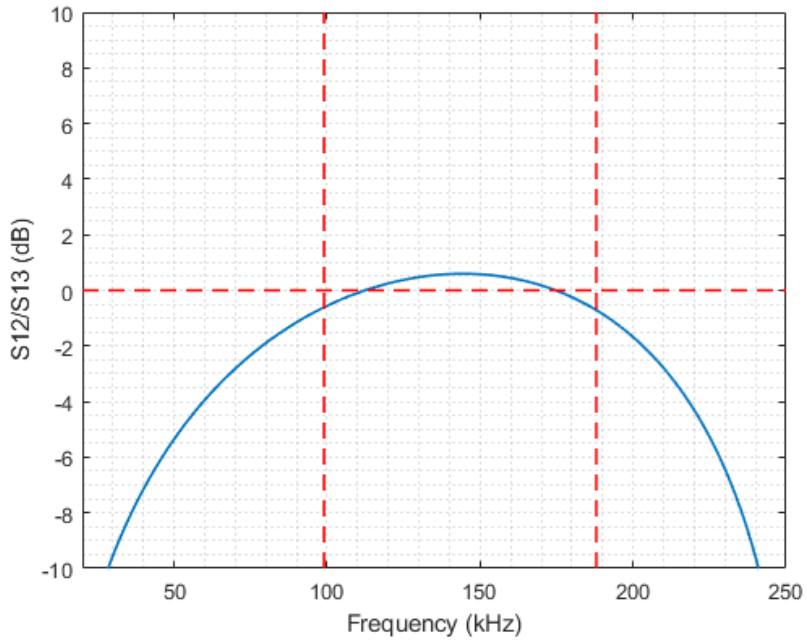

(a) Amplitude Imbalance

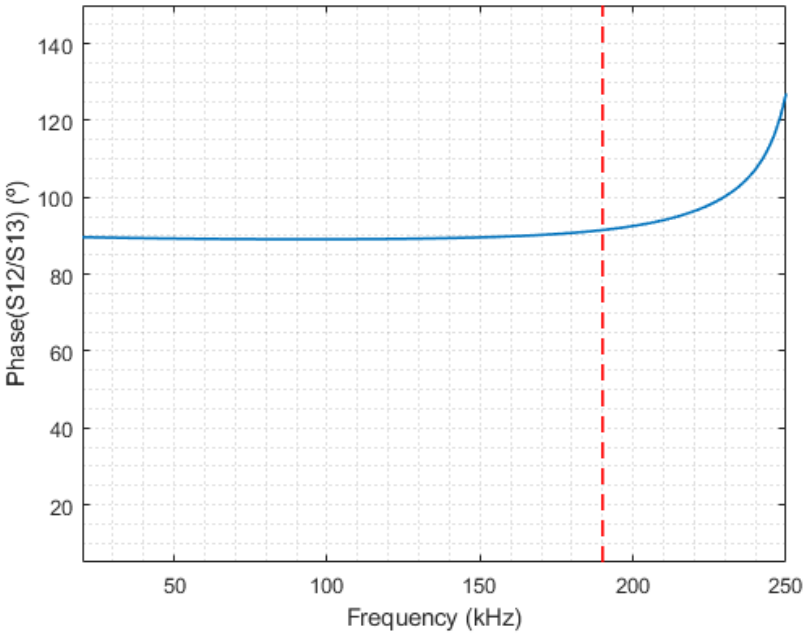

(b) Phase Imbalance

Figure 5.6: Simulation results of the transformer-based hybrid

Evidently for such a low frequency, the construction of this alternative model has also been carried out with the lumped element approach and as with the previous hybrid, the device has been implemented using FR4 substrate where component-landing layout has been milled. The

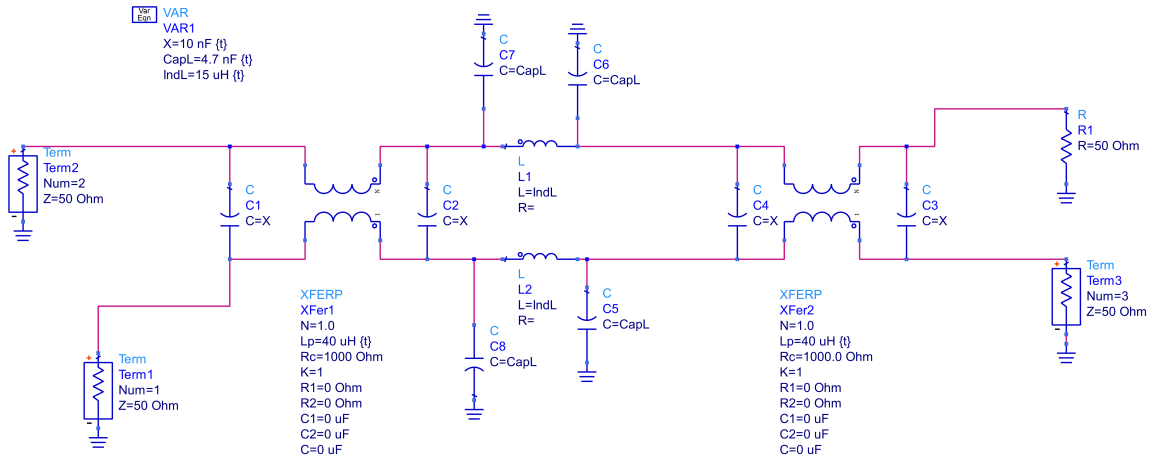

Figure 5.7: Schematic of the transformer-based hybrid coupler

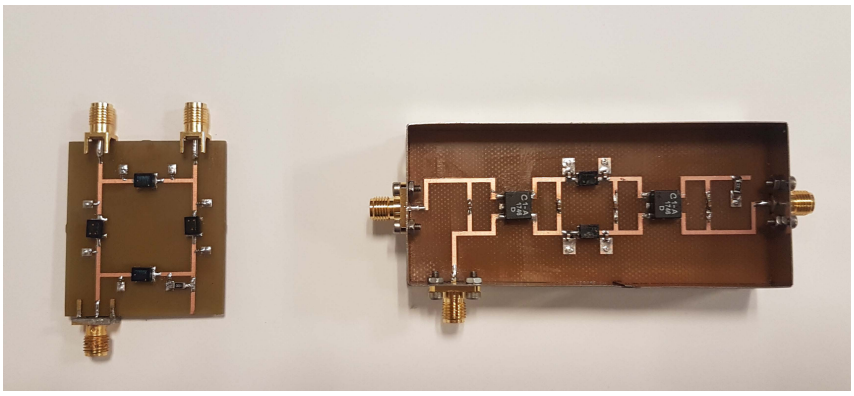

Figure 5.8: Lumped and transformer-based hybrid couplers

main results highlight a phase imbalance within specifications up to 190 kHz and a $\pm 0,5$ dB amplitude imbalance from 100 to 190 kHz. In order to protect the hybrid coupler, the device has been mounted inside a metal box and SMA ports have been attached. Figure 5.8 shows the physical implementation of this hybrid on the right-hand side.

5.2.3 Waveguide transition

In the presentation of this solution, the radiating elements of the proposed device are a pair of WR42 waveguide transitions that act as antennas. The gain of an open aperture can be approached using equation 5.5 [Car02] where a and b are the waveguide dimensions. In the case

of the WR42, $a = 10.7$ and $b = 4.3$ millimetres, what yields an approximate gain of 5.6 dBi.

$$D = \frac{4\pi ab}{\lambda^2} \tag{5.5}$$

The use of open rectangular waveguides as antenna elements, is not an optimal solution but fits the requirements of the initial tests in the anechoic chamber set-up. If a higher gain is desired, a pair of horn antennas can be attached to the waveguide flanges.

5.3 Prototype

The physical implementation of the emulator consists on a PVC box that contains the 4-port SSB and the pair of waveguide transitions connected to the LO and the RF ports. The IF ports are fed from the two outputs of the hybrid coupler and the original IF signal is generated using an Agilent N5183A analog signal generator. Picture 5.11 shows the final assembly of the prototype attached to the transformer-based hybrid coupler.

5.4 Experimental test

In order to test the constructed prototype of the emulator, the experiment has been set up in the anechoic chamber presented in chapter 4. The radar module and the reflector are kept at the DUT and probe pedestals respectively, and the emulator is mounted on a tripod on the absorbing walkway. Figure 5.12 shows the emulator module in the anechoic chamber.

Two different measurements from this set-up are depicted and the result of the first one is shown in figure 5.9. That figure depicts the range profile of the chamber set-up, using transmitter two and feeding the emulator with an IF tone of 180 kHz. See that a target appears at a range of 23 metres with a received power of $-99.3\ dBV$. Figure 5.10 depicts the range profile when an IF tone of a 100 kHz is used. Results are not completely as desired and need a thorough explanation.

In the case of a 180 kHz tone, the obtained emulated target is a double peak. This behaviour is caused by the amplitude imbalance of the hybrid at this frequency and therefore, the undesired sideband signal is not correctly rejected. Additionally in this figure a secondary peak at 48 metres is received due to the appearance of the mixer non-linearities. The effect of such non-linear behaviour is better shown in figure 5.10 where a tone of a 100 kHz is used. At this frequency, the amplitude balance of the hybrid is correct and the undesired sideband is rejected but secondary *ghost* targets appear. These targets correspond to the harmonic distortions added by the mixer at multiples of the desired frequency. In the previous case, the harmonics of the 180 kHz tone fell out of the emulating range and did not appear in the plot, but with the lowest

frequency, the harmonics are closely spaced. The appearance of such non-linear response is triggered by the fact that the biasing power of the mixer diodes is delivered via the IF ports due to the low power of the RF signal coming from the radar. In this experiment, an IF power of 8 dBm was needed and such high power enhances higher order products due to their larger slope.

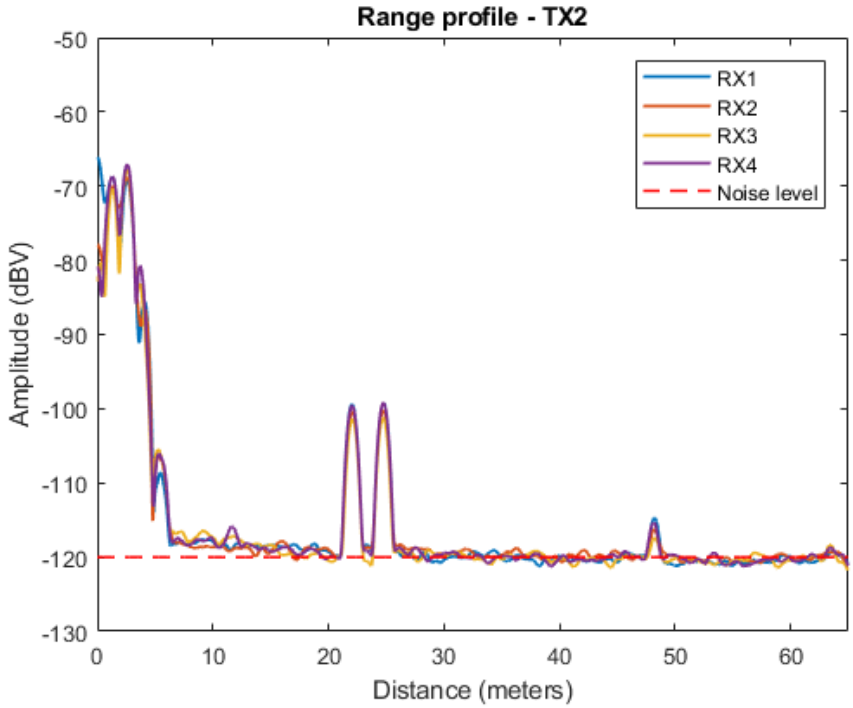

Figure 5.9: Range profile with emulated target at 23 metres

Finally, results of this experiment are encouraging but also a confirmation of new lines of study in this field. Range emulation has been achieved but two major problems need to be assessed: the imbalance of the hybrid is not correctly rejecting the lower-sideband thus yielding secondary targets, and the fact that the RF signal power is really low, forces the IF tone to be the power source for the mixer diodes. In order to tackle this second problem, different solutions are considered, for example, using horn antennas to increase gain or the use of a bias-tee stage on the IF ports so as to deliver the polarization power.

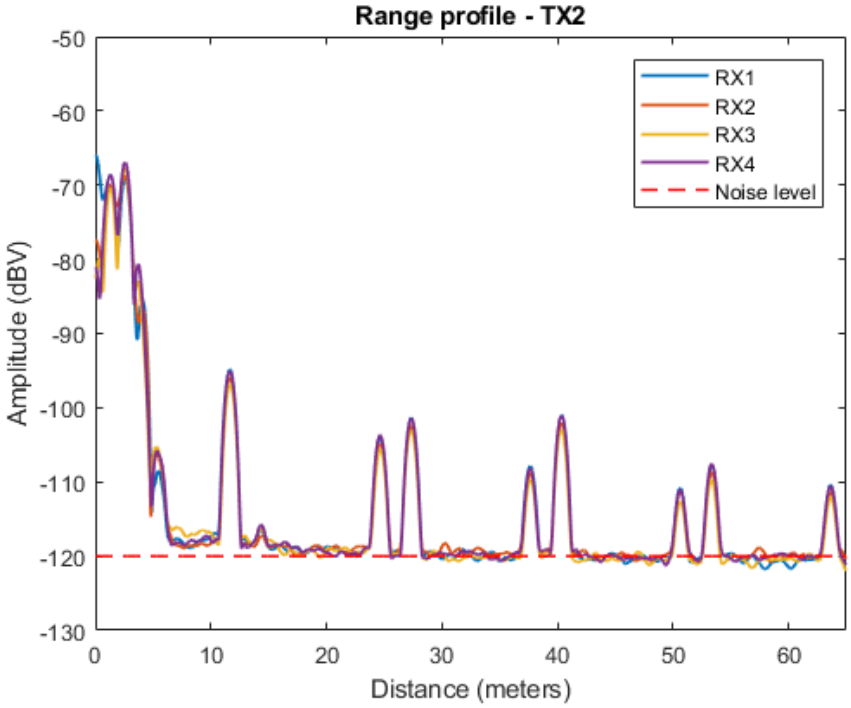

Figure 5.10: Range profile with an IF input of 100 kHz

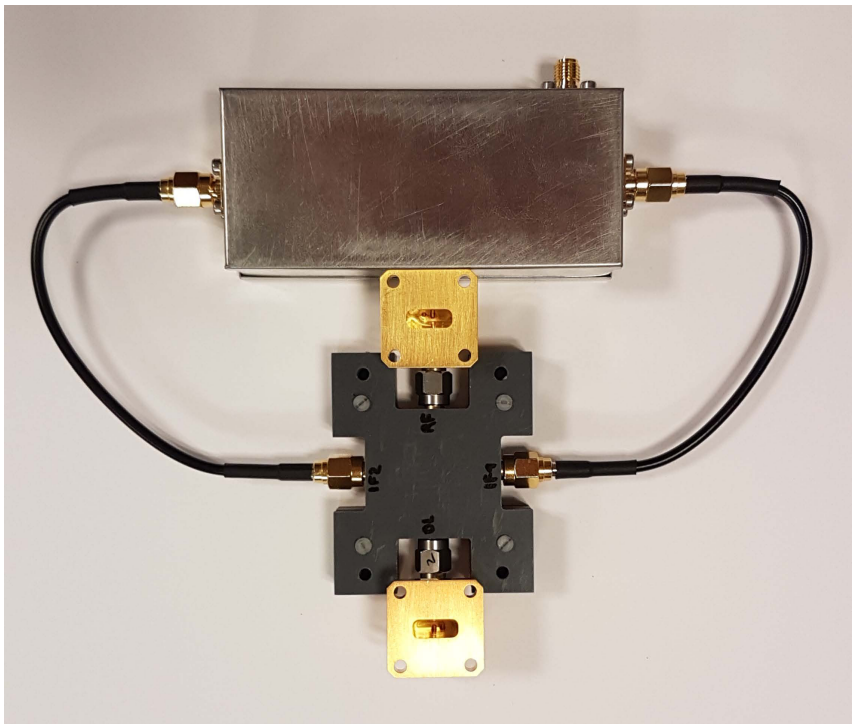

Figure 5.11: Emulator prototype

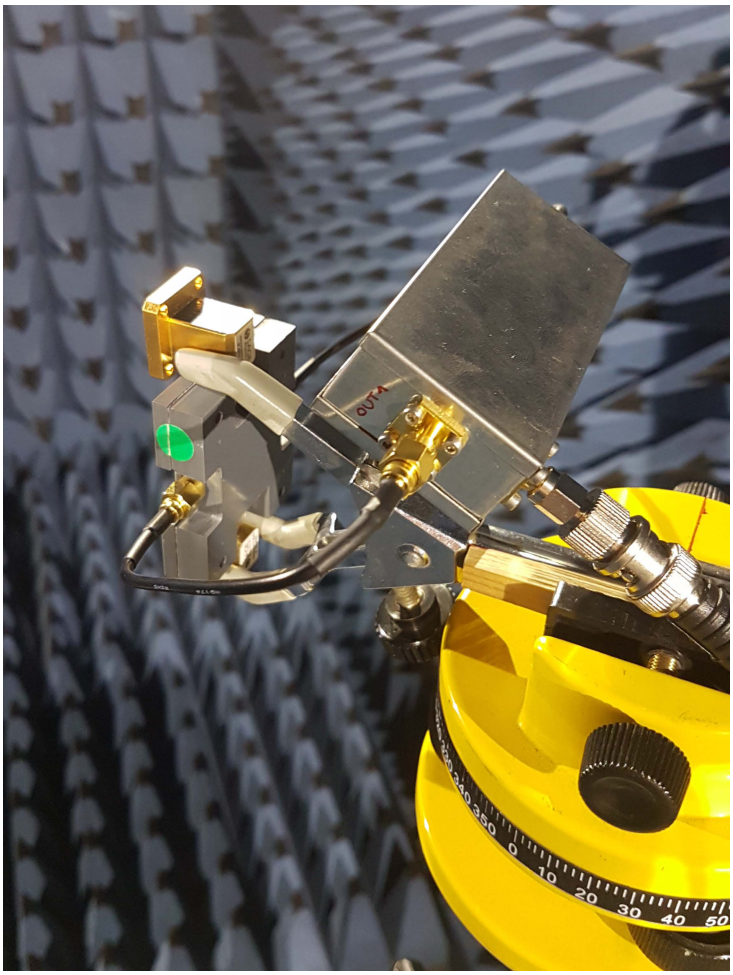

Figure 5.12: Side view of the emulation set-up

Chapter 6

Conclusions and future work

6.1 Conclusions

A market that pushes towards even safer vehicles and that labels automotive radar as a *killer application*, is driving technology to the finding of new solutions based on the presented frequency-modulated continuous-wave scheme. Automotive radar has been a field of study since the late 70's, but the solution was only deemed possible in luxury and top-notch vehicles. Now, with the increasing development of new low-cost devices and technologies, the scope has switched to a wide-market implementation of such systems under the umbrella of the *0 fatality* goal impulsed by governmental institutions. Thus, the market is in need of new low-cost solutions that ease any of the system development steps, and the trigger of this work is providing an introduction to the field from which further steps can be studied.

In the beginning, the deployment of the outlined DemoRad test board and the development of a core toolbox defining measurements and data analysis has been the main focus of this project. However, as more capabilities were discovered, new open lines were tackled including the design of a trihedral reflector and the idea behind the radar emulator. The intention was to provide a system-wide view through the whole process of the FMCW introduction because the interest laid in not only assessing the radar from a radio-frequency point of view but more of showing how the different disciplines in the field of telecommunications jointly conform a complex system.

In Chapter 2 a general introduction to the field of FMCW radar has been given and the well-known radar observables have been presented. This chapter represented the theoretical basis on which the forthcoming sections have been developed.

Chapter 3 is the general description and comprehension of the radar module that has been tested. Assessing how the system operated and providing a view of how the data is output was

the main objective at this point.

Chapters 4 and 5 represent the analysis of real radar operation. At the beginning of chapter four the definition of an experimental set-up arises some needs such as a characterized target and a controlled environment where measurements can be used to extract interesting results. The final result of the designed trihedral reflector, it being a non-calibrated device, and the fact that a hardware problem has been detected and reported to the provider, are points to remark in the development of chapter 4. In the end, the conception of a low-cost solution for radar testing and the physical implementation of the prototype have yielded interesting results that encourage a further study in this topic.

6.2 Future work

This project leaves a wide range of topics for further development and also some topics that would require a thorough study and that have been left open due to time limitations.

- In terms of the board under test, an even deeper study of the internal structure of the device would be interesting so as to clarify which are the hardware limitations of the system. Additionally, the development of an own USB interface and the phase drift that was detected during testing would require a further study from the hardware point of view.
- The real time operation of automotive radar systems has not been treated in this work but is a topic of major importance. From the DSP capabilities of the module, real-time target detection and mapping in interaction with other systems such as UAVs or small vehicles emerges as a potential project.
- Concerning the radar emulator, the simulation of targets with velocity has fallen out of the project because of time reasons but the actual implementation is feasible. Additionally, the optimal design of a pair of horn antennas, so to increase the power of the deceiving signal, and other hardware devices such as filters or amplifiers, might be a topic of interest.

There are also other topics that were considered when this work was proposed, that involve a deeper study of phase data recovered by the sensor. The interaction with vehicle radome structures or the need of low-cost alignment systems that can correct radar positions after vehicle damages are state-of-the-art topics to be developed. Finally, from the fact that the radar emulator is possible, the possibility of spoofing actual vehicles with mounted radars arises, presenting a new problem that must be studied.

Bibliography

[Bre09] Gary Breed, "Transmission line and lumped element quadrature couplers", *High Frequency Electronics*, 2009.

[Car02] Ángel Cardama, Lluís Jofre, Juan Manuel Rius, Jordi Romeu, Sebastián Blanc, Miguel Ferrando, *Antenas*, 2002.

[Coo17] Organization for Cooperation, Economic Development, *Road safety annual report*, chap. 36. Spain, OECD, 2017.

[Eng16] Maximilian Engelhardt, Florian Pfeiffer, Erwin Biebl, "A high bandwidth radar target simulator for automotive radar sensors", *Proceedings of the 13th European Radar Conference*, 2016.

[Fis73] R. E. Fisher, "Broad-band twisted-wire quadrature hybrids", *IEEE Trans. Microw. Theory Techn.*, 1973.

[Had15] Andreas Haderer, "Demorad (hardware user manual)", 2015.

[Ho89] Chen Y. Ho, Ge-Lih Chen, "Design of wideband quadrature couplers for uhf/vhf: Part 1", *RF Design*, 1989.

[INR17] INRAS, "Demorad-020600020085 calibration report", 2017.

[Kea17] Frank Kearney, Dave Frizelle, "Complex rf mixers, zero-if architecture and advanced algorithms", Tech. rep., Analog Devices, 2017.

[Lut14] Steffen Lutz, Christian Erhart, Thomas Walter, Robert Weigel, "Target simulator concept for chirp modulated 77 ghz automotive radar sensors", *Proceedings of the 11th European Radar Conference*, 2014.

[Mei14] Holger H. Meinel, "Evolving automotive radar - from the very beginnings into the future", Tech. rep., EuCAP, 2014.

[MVG16] "Pyramidal absorbers - aep series", 2016.

[PS18] Prof. Pedro de Paco Sánchez, "Lecture notes on automotive radar", 2018.

[Ram17] Karthik Ramasubramanian, "Moving from legacy 24 ghz to state-of-the-art 77 ghz radar", Tech. rep., Texas Instruments, 2017.

[Sar14] Tapan K. Sarkar, Magdalena Salazar Palma, "A history of the evolution of radar", *Proceedings of the 44th European Microwave Conference*, 2014.

[Sch17] Werner Scheiblhofer, Reinhard Feger, Andreas Haderer, Andreas Stelzer, "A low-cost multi-target simulator for fmcw radar system calibration and testing", *Proceedings of the 47th European Microwave Conference*, 2017.

[Sia18] Prof. Uwe Siart, "Lecture notes on radar signals and systems", 2018.

[Sko08] Merrill I. Skolnik, *Radar Handbook*, McGraw Hill, 3$^{\underline{\text{rd}}}$ ed., 2008.

[WHO15] World Health Organisation WHO, "Global status report on road safety (executive summary)", 2015.